

# Search for Spatially Extended *Fermi*-LAT Sources Using Two Years of Flight Data

J. Lande<sup>2,1</sup>, S. Funk<sup>2,1</sup>, M. Ackermann<sup>3,1</sup>, ...

## ABSTRACT

Spatial extension is an important characteristic for correctly associating LAT sources with their counterparts at other wavelengths and for obtaining an unbiased model of their spectra. We present a new method for quantifying the spatial extension of sources detected by the Large Area Telescope (LAT), the primary science instrument on the *Fermi Gamma-ray Space Telescope* (*Fermi*). We perform a series of Monte Carlo simulations to validate this tool and calculate the LAT threshold for detecting the spatial extension of sources. We then test all sources in the second *Fermi*-LAT catalog (2FGL) for extension. **We report the detection of seven spatially extended sources in addition to the twelve spatially extended sources reported in 2FGL and two others studied in dedicated publications.**

*Subject headings:* Catalogs; Fermi Gamma-ray Space Telescope; Gamma rays: observations; ISM: supernova remnants; Methods: statistical; pulsar wind nebula

## 1. Introduction

A number of astrophysical source classes including supernova remnants (SNRs), pulsar wind nebulae (PWNe), molecular clouds, normal galaxies, and galaxy clusters are expected to be spatially resolvable at GeV energies. Dark matter satellites are also hypothesized to be spatially extended. The Large Area Telescope (LAT) on the *Fermi Gamma-ray Space Telescope* (*Fermi*) has detected seven SNRs which are significantly extended at GeV energies: W51C, W30, IC443, W28, W44, RX J1713.7–3946, and the Cygnus Loop (Abdo et al.

---

<sup>1</sup>Corresponding authors: M. Ackermann, markus.ackermann@desy.de; S. Funk, funk@slac.stanford.edu; J. Lande, joshualande@gmail.com.

<sup>2</sup>W. W. Hansen Experimental Physics Laboratory, Kavli Institute for Particle Astrophysics and Cosmology, Department of Physics and SLAC National Accelerator Laboratory, Stanford University, Stanford, CA 94305, USA

<sup>3</sup>Deutsches Elektronen Synchrotron DESY, D-15738 Zeuthen, Germany

2009b, 2011c, 2010i,e,h, 2011e; Katagiri et al. 2011). In addition, three PWNe were detected as being extended: MSH 15–52, Vela X, and HESS J1825–137 (Abdo et al. 2010a,f; Grondin et al. 2011). Two close-by galaxies, the Large and Small Magellanic Clouds, and one radio galaxy, Centarus A, were spatially resolved at GeV energies (Abdo et al. 2010j,b,c). A number of additional sources detected at GeV energies are positionally coincident with sources that exhibit extension at other wavelengths, large enough to be spatially resolvable by the LAT at GeV energies.

The current generation of air Cherenkov detectors have made it apparent that many sources can be spatially resolved at even higher energies. Most prominent was a survey of the Galactic plane using the High Energy Stereoscopic System (H.E.S.S) which reported 14 spatially extended sources with extensions varying from  $\sim 0^\circ.1$  to  $\sim 0^\circ.25$  (Aharonian et al. 2006). In fact, within our Galaxy only very few sources detected at TeV energies (most notably the  $\gamma$ -ray binaries LS 5039 (Aharonian et al. 2006a), LS I+61–303 (Albert et al. 2006; Acciari et al. 2011), HESS J0632+057 (Aharonian et al. 2007c), and the Crab nebula (Weekes et al. 1989)) have no detectable extension. High-energy  $\gamma$ -rays from these sources are produced by the decay of  $\pi^0$ s produced by hadronic interactions with interstellar matter and by relativistic electrons due to Inverse Compton (IC) scattering and Bremsstrahlung radiation. It is plausible that the GeV and TeV emission from these sources originates from the same population of high-energy particles and so at least some of these sources should be detected at GeV energies. Studying these TeV sources at GeV energies would help to determine the emission mechanisms producing these high energy photons.

The LAT is a pair conversion telescope that has been surveying the  $\gamma$ -ray sky since 2008 August. The LAT has broad energy coverage (20 MeV to  $> 300$  GeV), wide field of view ( $\sim 2.4$  sr), and large effective area ( $\sim 8000$  cm<sup>2</sup> at  $> 1$  GeV). Additional information about the performance of the LAT can be found in Atwood et al. (2009). Using 2 years of all-sky surveying data, the LAT Collaboration published a catalog of 1873 sources significantly detected at GeV energies called 2FGL (Abdo et al. 2011d). The possible counterparts of many of these sources can be spatially resolved when observed at other frequencies but detecting the spatial extension of these sources at GeV energies is difficult because the size of the point-spread function (PSF) of the LAT is comparable to the typical size of many of these sources.

The capability to spatially resolve GeV  $\gamma$ -ray sources is important for several reasons. Finding a coherent source extension across different energy bands can help to associate a LAT source to an otherwise confused counterpart. Furthermore, some of the dark matter substructure in our Galaxy is predicted to be spatially extended at GeV energies (Baltz et al. 2008). Characterization of spatial extension could help to identify this substructure. Also, due to

the strong energy dependence of the LAT PSF, the spatial and spectral characterization of a source cannot be decoupled. An inaccurate spatial model will bias the spectral model of the source and vice versa. Specifically, modeling a spatially extended source as point-like will systematically shift a spectral analysis to softer indices. Furthermore, correctly modeling source extension is important for understanding an entire region of the sky. For example, an imperfect model of the spatially extended LMC introduced significant residuals in the surrounding region (Abdo et al. 2010d, 2011d). Such residuals can bias the significance and measured spectrum of neighboring sources in the densely populated Galactic plane.

**Previous analysis of extended LAT sources was performed as dedicated studies of individual sources so we expect that a systematic scan of all LAT detected sources could uncover additional spatially extended sources. For these reasons, in Section 2 we present a new systematic method for analyzing spatially extended LAT sources. In Section 3, we demonstrate that this method can be used to test the statistical significance of the extension of a LAT source and in Section 4 we calculate the LAT detection threshold to resolve the extension of a source. In Section 5, we study the ability of the LAT to distinguish between a spatially extended source and the confusion of nearby point-like sources. In Section 6, we further demonstrate that our detection method does not misidentify point-like sources as being extended by testing the extension of active galactic nuclei (AGN) believed to be unresolvable. In Section 7, we systematically reanalyze the twelve extended sources included in 2FGL and in Section 8 we describe a way to estimate systematic errors on the extension of a source. In Section 9, we describe a search for new spatially extended LAT sources. Finally, in Section 10 we present the detection of the extension of nine spatially extended sources that were reported in 2FGL but as being point-like. Two of these sources have been previously analyzed in dedicated publications.**

## 2. Analysis Methods

Morphological studies of sources using the LAT are challenging because of the strongly energy-dependent PSF that is comparable in size to the extension of many sources expected to be detected at GeV energies. Additional complications arise for sources along the Galactic plane due to systematic uncertainties in the Galactic diffuse emission. The LAT PSF is limited at its lowest detectable energies by multiple scattering in the silicon strip tracking section of the detector and is several degrees at 100 MeV. The PSF improves with energy approaching a 68% containment radius of  $\sim 0.2^\circ$  at the highest energies (when averaged over

the acceptance of the LAT) and is limited by the granularity of the silicon strips in the tracker (Atwood et al. 2009; Abdo et al. 2009e, 2011a).<sup>1</sup> However, since most high energy astrophysical sources have spectra that decrease rapidly with increasing energy, there are typically fewer higher energy photons with improved angular resolution. Therefore sophisticated analysis techniques are required to maximize the LATs sensitivity to these extended sources.

## 2.1. The pointlike Package

A new analysis tool has been developed to address the unique requirements for studying spatially extended sources with the LAT. The Poisson likelihood to find the observing counts is maximized given a parametrized spatial and spectral model of the source and its surrounding region. The sky is divided into cubes of space and energy using the healpix representation of the sky (Górski et al. 2005) and the likelihood is maximized over all bins in a region. The extension of a source can be modeled by a geometric shape (e.g. a disk or a two-dimensional Gaussian) and the source’s position, extension, and spectrum can be simultaneously fit.

This type of analysis is not feasible using the standard LAT likelihood analysis tool `gtlike`<sup>2</sup> because it can only fit the spectral parameters of the model unless a more sophisticated iterative procedure is used to also test various source morphologies. We note that `gtlike` has been used in the past in several studies of source extension in the LAT Collaboration (Abdo et al. 2010j,b,e, 2009b). In these studies, a profile based upon a set of `gtlike` maximum likelihood fits at fixed extensions was used to build a profile of the likelihood as a function of extension. This approach is not optimal because the position, extension, and spectrum of the source must be simultaneously fit to find the best fit parameters and to maximize the statistical significance of the detection. Furthermore since the `gtlike` likelihood profile approach is computationally intensive, no large-scale Monte Carlo simulations have been run to validate it.

The approach presented here is based on a second maximum likelihood fitting package developed in the LAT Collaboration called `pointlike` (Abdo et al. 2010d; Kerr 2011). The choice to base the spatial extension fitting on `pointlike` rather than `gtlike` was made on considerations of computing time. The `pointlike` algorithm was optimized for speed

---

<sup>1</sup>More information about the performance of the LAT can be found at the *Fermi* Science Support Center (FSSC, <http://fermi.gsfc.nasa.gov>).

<sup>2</sup>`gtlike` is distributed publicly by the FSSC.

115 to handle larger numbers of sources efficiently, which is important for our catalog scan  
 116 and for being able to perform large-scale Monte Carlo simulations to validate the analysis.  
 117 Details on the `pointlike` package can be found in Kerr (2011). We extended the code to  
 118 allow a simultaneous fit of the source extension together with the position and the spectral  
 119 parameters.

## 2.2. Extension Fitting

120  
 121 In `pointlike`, it is assumed that the spatial and spectral model of an extended source are  
 122 separable, i.e. that the source model  $M(l, b, E) = S(l, b) \times X(E)$  where  $S(l, b)$  is the spatial  
 123 distribution and  $X(E)$  is the spectral distribution. To fit an extended source, `pointlike`  
 124 convolves the extended source shape with the PSF (as a function of energy) and uses the  
 125 `minuit` library (James & Roos 1975) to maximize the likelihood by simultaneously varying  
 126 the position, extension, and spectrum of the source. As will be described in Section 3,  
 127 simultaneously fitting the position, extension, and spectrum is important to maximize the  
 128 statistical significance of the detection of extension of a source. To avoid projection effects,  
 129 the source’s longitude and latitude are not directly fit but instead the source’s displacement  
 130 in a rotated reference frame.

The significance of the extension of a source can be calculated from the likelihood ratio  
 test of a hypothesis with a spatially extended source and a hypothesis with a point-like  
 source. The test statistic for this procedure is defined as

$$\text{TS}_{\text{ext}} = 2 \log(\mathcal{L}_{\text{ext}}/\mathcal{L}_{\text{ps}}) \quad (1)$$

131 where  $\mathcal{L}$  is the Poisson likelihood. `pointlike` calculates  $\text{TS}_{\text{ext}}$  by fitting a source first with  
 132 a spatially extended model and then as a point-like source. The interpretation of  $\text{TS}_{\text{ext}}$  in  
 133 terms of a statistical significance is discussed in Section 3.

For extended sources with an assumed radially-symmetric shape, we optimized the cal-  
 culation by performing one of the integrals analytically. The expected photon distribution  
 can be written as

$$\text{PDF}(\vec{r}) = \int \text{PSF}(|\vec{r} - \vec{r}'|) I_{\text{src}}(\vec{r}') r' dr' d\phi' \quad (2)$$

where  $I_{\text{src}}(\vec{r}')$  is the spatial distribution of the source. For the LAT, the PSF can be param-  
 eterized by a King function (King 1962):

$$\text{PSF}(r) = \frac{1}{2\pi\sigma^2} \left(1 - \frac{1}{\gamma}\right) \left(1 + \frac{u}{\gamma}\right)^{-\gamma}, \quad (3)$$

where  $u = (r/\sigma)^2/2$  and  $\sigma$  and  $\gamma$  are free parameters (Kerr 2011). For radially-symmetric extended sources, the angular part of the integral can be evaluated analytically

$$\begin{aligned} \text{PDF}(u) &= \int_0^\infty r' dr' I_{\text{src}}(v) \int_0^{2\pi} d\phi' \text{PSF}(\sqrt{2\sigma^2(u + v - 2\sqrt{uv} \cos(\phi - \phi'))}) \\ &= \int_0^\infty dv I_{\text{src}}(v) \left( \frac{\gamma - 1}{\gamma} \right) \left( \frac{\gamma}{\gamma + u + v} \right)^\gamma \times {}_2F_1 \left( \gamma/2, \frac{1 + \gamma}{2}, 1, \frac{4uv}{(\gamma + u + v)^2} \right). \end{aligned} \quad (4)$$

where  $v = (r'/\sigma)^2/2$  and  ${}_2F_1$  is the Gaussian hypergeometric function. This convolution formula reduces the expected photon distribution to a single numerical integral.

There will always be a small numerical discrepancy between the expected photon distribution derived from a true point-like source and a very small extended source due to numerical error in the convolution. In most situations, this error is insignificant. But in particular for very bright sources, this numerical error has the potential to bias the test statistic for the extension test. Therefore, when calculating  $\text{TS}_{\text{ext}}$ , we compare the likelihood fitting the source with an extended spatial model to the likelihood when the extension is fixed to a very small value ( $10^{-10}$  degrees in radius for a uniform surface brightness profile).

We estimate the error on the extension of a source by fixing the position of the source and varying the extension until the likelihood has fallen by  $\frac{1}{2}$ , corresponding to a  $1\sigma$  error (Eadie et al. 1971). Figure 1 demonstrates this method by showing the change in the log of the likelihood when varying the extension of the SNR IC443. The localization error is calculated by fixing the extension and spectrum of the source to their best fit value and then fitting to the likelihood function a 2D Gaussian as a function of position. This localization error algorithm is further described in Abdo et al. (2011d).

### 2.3. gtlike Analysis Validation

**pointlike** is important for LAT analyses that require many iterations such as source localization and extension fitting. On the other hand, because **gtlike** makes fewer approximations in calculating the likelihood we expect the spectral parameters found with **gtlike** to be slightly more precise. Furthermore, because **gtlike** is the standard likelihood analysis package, it has been more extensively validated for spectral analysis. For those reasons, in the following analysis we used **pointlike** to determine the position and extension of a source and subsequently derived the spectrum using **gtlike**. Both **gtlike** and **pointlike** can be used to estimate the statistical significance of the extension of a source and we required that both methods agree for a source to be considered extended. There was good agreement between the two methods. Unless explicitly mentioned, all TS,  $\text{TS}_{\text{ext}}$ , and spectral parameters

161 were calculated using `gtlike` with the best-fit positions and extension found by `pointlike`.

## 162 2.4. Comparing Source Sizes

We considered two different models that can be used to model the surface brightness profile for extended sources, either a 2D Gaussian profile

$$I_{\text{Gaussian}}(x, y) = \frac{1}{2\pi\sigma^2} \exp(-(x^2 + y^2)/2\sigma^2) \quad (6)$$

or a uniform surface brightness profile

$$I_{\text{disk}}(x, y) = \begin{cases} \frac{1}{\pi\sigma^2} & x^2 + y^2 \leq \sigma^2 \\ 0 & x^2 + y^2 > \sigma^2. \end{cases} \quad (7)$$

163 Although these shapes are significantly different, Figure 2 shows that their PDF  
 164 are similar for a source that has a 0.5 radius typical of LAT detected extended  
 165 sources. To allow a valid comparison between the Gaussian and the uniform  
 166 surface brightness morphologies, we define the source size as the radius contain-  
 167 ing 68% of the intensity ( $r_{68}$ ).  $r_{68, \text{Gaussian}} = 1.51\sigma$  and  $r_{68, \text{disk}} = 0.82\sigma$  where  $\sigma$  is  
 168 defined in Equation 6 and Equation 7 respectively. For this example,  $r_{68} = 0.5$  so  
 169  $\sigma_{\text{disk}} = 0.61^\circ$  and  $\sigma_{\text{Gaussian}} = 0.33^\circ$ .

170 For smaller and fainter extended sources, the differences in the PDF for  
 171 different spatial models lost in the noise and the LAT is not sensitive to the  
 172 detailed spatial structure of these sources. Therefore, in our search for extended  
 173 sources we use only a radially-symmetric uniform surface brightness profile as  
 174 our spatial extension shape. Unless otherwise noted, we quote the radius of the  
 175 edge ( $\sigma$ ) as the size of the source.

## 176 3. Validation of Analysis Method

We tested the false detection probability for the extended source test by fitting the extension of point-like sources. Mattox et al. (1996) discuss that the test statistic distribution for a likelihood ratio test on the existence of a source at a given position is

$$P(\text{TS}) = \frac{1}{2}(\chi_1^2(\text{TS}) + \delta(\text{TS})). \quad (8)$$

177 The particular form of Equation 8 is due to the null hypothesis (source flux  $\Phi = 0$ ) residing  
 178 on the edge of parameter space and the model hypothesis adding a single degree of freedom



and leads to the often quoted result that the square root of the test statistic is the number of  $\sigma$  of the detection. It is plausible to expect a similar distribution of the test statistic in the test for source extension since the same conditions apply (with the source flux  $\Phi$  replaced by the source radius  $r$  and  $r < 0$  being unphysical). We performed Monte Carlo simulations to calculate empirical distributions for  $\text{TS}_{\text{ext}}$  and we compared them to Equation 8.

We simulated point-like sources with various spectral forms using the LAT on-orbit simulation tool `gtobssim`<sup>3</sup> and fit the sources with `pointlike` using both point-like and extended source hypotheses. These point-like sources were simulated with a power-law spectral model with integrated fluxes above 100 MeV ranging from  $3 \times 10^{-9}$  to  $1 \times 10^{-6}$   $\text{ph cm}^{-2} \text{s}^{-1}$  in six discrete steps and spectral indices ranging from 1.5 to 3 in four discrete steps. These values were picked to represent typical source parameters of LAT-detected sources. The point-like sources were simulated on top of an isotropic background with a power-law spectral model with integrated flux above 100 MeV of  $1.5 \times 10^{-5}$   $\text{ph cm}^{-2} \text{s}^{-1}$  and spectral index 2.1. This was taken to be the same as the isotropic spectrum measured by EGRET (Sreekumar et al. 1998). The Monte Carlo simulation was performed over a one-year observation period using a representative rocking profile and a representative livetime fraction of 0.8. The reconstruction was performed using photons with energies between 1 GeV and 100 GeV and the Pass 7\_V6 (P7\_V6) Source Instrument Response Function (IRFs, Abdo et al. (2011a)). For each significantly detected point-like source ( $\text{TS} \geq 25$ ), we used `pointlike` to fit the source as an extended source and calculate  $\text{TS}_{\text{ext}}$ .

For each set of spectral parameters,  $\sim 30,000$  statistically independent simulations were performed. For dimmer spectral models, many of the simulations left the source undetected ( $\text{TS} < 25$ ) and were discarded. Table 1 shows the different spectral models used in our study as well as the number of simulations and the average point-like source significance. The cumulative density of  $\text{TS}_{\text{ext}}$  is plotted in Figure 3 and compared to the  $\chi^2_1/2$  distribution of Equation 8.

**Our study shows broad agreement between simulations and Equation 8. Nevertheless, the agreement is not perfect. It should be noted that the discrepancy seems to be worst for softer sources where we are anyways less sensitive to the source’s extension. One possible reason for departures from Equation 8 is that pointlike ignores energy dispersion which will change the PSF shape as a function of energy. Considering the distribution in Figure 3, the choice of a threshold set to 16 (correspond to a  $4\sigma$  detection if Equation 8 strictly held) is reasonable despite the imperfections of the corresponding calibration.**

---

<sup>3</sup>`gtobssim` is distributed publicly by the FSSC.



#### 4. Extended Source Detection Threshold

We calculated the LAT flux threshold to detect that a spatially extended source is extended. We define the detection threshold as the flux at which the value of  $\text{TS}_{\text{ext}}$  averaged over many statistical realizations is  $\langle \text{TS}_{\text{ext}} \rangle = 16$  for a source of a given flux and true extension.

We used a simulation setup similar to that described in Section 3, but instead of point-like sources we simulated extended sources with a radially-symmetric uniform surface brightness profile. Additionally, we simulated our sources over the two-year time range included in 2FGL. For each extension and spectral index, we selected a flux range which bracketed  $\text{TS}_{\text{ext}} = 16$  and performed an extension test for  $> 100$  independent realizations of ten fluxes in the range. We calculated  $\langle \text{TS}_{\text{ext}} \rangle = 16$  by fitting a line to the flux and  $\text{TS}_{\text{ext}}$  values in the narrow range.

Figure 4 shows the threshold for sources of four spectral indices from 1.5 to 3 and extensions varying from  $\sigma = 0.1$  to  $2.0$ . The LAT flux threshold for a significant detection of source extension drops quickly with increasing source size and reaches a minimum around  $0.5$ . **The threshold is high for small extensions when the source is small compared to the size of the PSF. The threshold increases for large extended sources because the source becomes increasingly diluted by the background.** Figure 4 shows the threshold using photons with energies between 100 MeV and 100 GeV and also using only photons with energies between 1 GeV and 100 GeV. Except for very large or very soft sources, our detection threshold is not substantially improved by including photons with energies between 100 MeV and 1 GeV. This is also demonstrated in Figure 1 which shows  $\text{TS}_{\text{ext}}$  for the SNR IC443 computed independently in twelve energy bins between 100 MeV and 100 GeV. For IC443, which has a spectral index  $\sim 2.4$  and an extension  $\sim 0.35$ , almost the entire increase in likelihood modeling the source as being extended comes from energies above 1 GeV. Furthermore, other systematic errors become increasingly important at low energy. For our extension search (Section 9), we therefore used only photons with energies above 1 GeV.

Figure 5 shows the flux threshold as a function of source extension for different background levels ( $1\times$ ,  $10\times$ , and  $100\times$  the nominal background), different spectral indices, and two different energy ranges (1 GeV to 100 GeV and 10 GeV to 100 GeV). The detection threshold is higher for sources in regions of higher background. When studying sources only at energies above 1 GeV, the LAT detection threshold (defined as the 1 GeV to 100 GeV flux at which  $\langle \text{TS}_{\text{ext}} \rangle = 16$ ) depends less strongly on the source’s spectral index. **The index dependence of the detection threshold is even weaker when considering only photons with energies above 10 GeV because the PSF changes little from 10**

**GeV to 100 GeV.** Overlaid on Figure 5 are the LAT detected extended sources that will be discussed in Sections 7 and 10. The extension thresholds are tabulated in Table 2.

Finally, Figure 6 shows the projected detection threshold of the LAT to extension with a 10 year exposure against 10 times the isotropic background measured by EGRET. This background is representative of the background near the Galactic plane. For small extended sources, our detection threshold improves by a factor larger than the square root of the exposure because at high energies, where we are most sensitive to extension, the background levels are in the Poisson instead of the Gaussian regime. For large extended sources, the relevant background is over a larger spatial range and so the improvement is closer to the expected factor corresponding to the square root of the exposure.

## 5. Testing Against Source Confusion

**It is impossible to discriminate with LAT data exclusively between a spatially extended source and multiple point-like sources separated by angular distances comparable to or smaller than the size of the LAT PSF. To assess the plausibility of source confusion for situations in which  $TS_{\text{ext}} > 16$ , we developed an algorithm in pointlike to simultaneously fit the position and spectrum of two point-like sources.**

After simultaneously fitting the two positions and two spectra, we define  $TS_{2\text{pts}}$  as twice the increase in the log of the likelihood fitting the region as two point-like sources compared to fitting the region as one point-like source:

$$TS_{2\text{pts}} = 2 \log(\mathcal{L}_{2\text{pts}}/\mathcal{L}_{\text{ps}}). \quad (9)$$

$TS_{2\text{pts}}$  cannot be quantitatively compared to  $TS_{\text{ext}}$  using a simple likelihood ratio test to evaluate which model is significantly better because the models are not nested (Protassov et al. 2002). Even though the comparison of  $TS_{\text{ext}}$  with  $TS_{2\text{pts}}$  is not a calibrated test,  $TS_{\text{ext}} > TS_{2\text{pts}}$  indicates that the likelihood for the extended source hypothesis is higher than for two point-like sources and we only consider a source to be extended if  $TS_{\text{ext}} > TS_{2\text{pts}}$ .

We assessed the power of the  $TS_{\text{ext}} > TS_{2\text{pts}}$  test with a Monte Carlo study. We simulated one spatially extended source and fit it as both an extended source and as two point-like sources. We then simulated two point-like sources and fit them with the same two hypothesis. By comparing the distribution of  $TS_{2\text{pts}}$  and  $TS_{\text{ext}}$  for the two cases, we evaluated how well the  $TS_{\text{ext}} > TS_{2\text{pts}}$  test is at rejecting the possibility of source confusion as well as how likely it is to

incorrectly reject with this test that an extended source is spatially extended. All sources were simulated using the same two-year time range included in 2FGL and all fit values were calculated using pointlike. The simulations were performed against an background 10 times the isotropic background measured by EGRET, representative of the background near the Galactic plane.

We did this study first in the energy range from 1 GeV to 100 GeV by simulating extended sources of flux  $4 \times 10^{-9} \text{ph cm}^{-2} \text{s}^{-1}$  integrated from 1 GeV to 100 GeV with a power-law spectral model with spectral index 2. This flux was picked to be representative of the new extended sources that were discovered in the following analysis when looking in the 1 GeV to 100 GeV energy range (see Section 10). We simulated these sources using a uniform surface brightness profile with extensions varying up to  $1^\circ$ . Figure 7a shows the distribution of  $\text{TS}_{2\text{pts}}$  and  $\text{TS}_{\text{ext}}$  as a function of the simulated extension of the source for 200 statistically independent simulations.

Figure 7c shows the same analysis but when fitting simulations of two point-like sources each with half of the flux of the spatially extended source and with the same spectral index as the extended source. Finally, figure 7e shows the same analysis with each point-like source having the same flux but different spectral indices. One point-like source had a spectral index of 1.5 and the other an index of 2.5.

The same three plots are shown in figure 7b, figure 7d, and figure 7f but this time when analyzing a source of flux  $10^{-9} \text{ph cm}^{-2} \text{s}^{-1}$  (integrated from 10 GeV to 100 GeV) only in the 10 GeV to 100 GeV energy range. This spectrum is typical of the new extended sources discovered using only photons with energies between 1 GeV and 100 GeV (see Section 10).

Several interesting conclusions can be made from this study. The overall behavior of these plots is what one would expect.  $\text{TS}_{\text{ext}}$  is on average greater than  $\text{TS}_{2\text{pts}}$  when fitting simulated extended sources whereas  $\text{TS}_{2\text{pts}}$  is greater than  $\text{TS}_{\text{ext}}$  when fitting two simulated point-like sources. Furthermore, the distributions of  $\text{TS}_{\text{ext}}$  and  $\text{TS}_{2\text{pts}}$  separate better when the extended source is bigger or when the two point-like sources are farther apart.

The distributions also shows that for simulated extended sources with typical sizes ( $\sigma \sim 0.5$ ), one can often obtain almost as good an increase in likelihood when fitting the extended source as two point-like sources. This is because although two point-like sources represent an incorrect spatial model, the two

point-like sources have four additional degrees of freedom (two spatial and two spectral parameters) than one extended source (one extension parameter) and can therefore easily model the extended source and statistical fluctuations in the data. This effect is most pronounced when using photons with energies between 1 GeV and 100 GeV where the PSF is even larger. On the other hand, when testing the two simulated point-like sources for extension our test did a better job at separating the distribution of  $TS_{2pts}$  and  $TS_{ext}$  and found that  $TS_{2pts}$  was typically much larger than  $TS_{ext}$ . This is because the one additional extension parameter is less able to model the second source or statistical fluctuations.

From this, we conclude that the  $TS_{ext} > TS_{2pts}$  test is powerful at discarding cases in which the true emission is derived from two point-like sources instead of from a spatially extended source. On the other hand, because of the large values of  $TS_{2pts}$  in figure 7a and figure 7b when fitting spatially extended sources, we caution that even in the case of their being spatially extended emission the fit of two point-like sources can often seem (by comparing the likelihoods) to be almost as good.

Finally, figure 8 shows the absolute value of the difference of the fit spectral indices for the case of fitting simulated spatially extended sources as two point-like sources. The plot compares the fit in the 1 GeV to 100 GeV energy range and in the 10 GeV to 100 GeV energy range. An error on the difference in spectral index is calculated by adding in quadrature the statistical errors on the spectral indices. This plot shows that there can be a large difference in the spectral index of the two fit point-like sources which is often greater than the statistical errors on the difference in spectral index. This is because the fit values the errors on an incorrect model are not expected to be meaningful. Therefore, the difference in spectral index when fitting an extended source candidate as two point-like sources can not be easily used to help determine whether a source is actually spatially extended instead of being the emission of two nearby point-like sources.

From this Monte Carlo study, we can see the limits of a LAT analysis of spatially extended sources. Section 3 showed that we have a statistical test that finds when a LAT source is not well described by the PSF. But this test does not uniquely prove that the emission originates from spatially extended emission instead of from multiple unresolved sources. Demanding that  $TS_{ext} > TS_{2pts}$  is a powerful second test to avoid cases of simple confusion of two point-like sources. But it could always be the case that an extended source candidate is actually the

superposition of multiple point-like or extended sources that could be resolved with deeper observations of the region. There is nothing about this conclusion unique to LAT analysis, but the larger PSF of the LAT and the density of sources expected to be GeV emitters in the galactic plane makes this issue more significant for LAT analysis. When possible, multiwavelength information should be used to help select the best model of the sky.

Even though this dedicated monte carlo study was performed using pointlike, for the analysis of LAT data we took the best fit positions of the two point-like sources and refit them using gtlike. We quote  $TS_{2pts}$  calculated with gtlike using the best fit positions of the two point-like sources found using pointlike.

## 6. Test of 2LAC Sources

For all following LAT analysis, we used the same two-year dataset that was used in 2FGL spanning from 2008 August 4 to 2010 August 1. We applied the same acceptance cuts and we used the same P7\_V6 Source class event selection and IRFs (Abdo et al. 2011a). When analyzing sources in pointlike, we used a circular  $10^\circ$  region of interest (ROI) centered on our source. When refitting the region in gtlike using the best fit spatial and spectral models from pointlike, we used the ‘binned likelihood’ mode of gtlike on a  $14^\circ \times 14^\circ$  ROI with a pixel size of  $0.03^\circ$ .

Unless explicitly mentioned, we used the same background model as 2FGL to represent the Galactic diffuse, isotropic, and Earth limb emission. To account for possible residuals in the diffuse emission model, the galactic emission was scaled by a power-law and the isotropic component’s normalization was left free. Unless explicitly mentioned, we used all 2FGL sources within  $15^\circ$  of our source as our list of background sources and we refit the spectral parameters of all sources within  $2^\circ$  of the source.

To validate our method, we tested LAT sources associated with AGN for extension. GeV emission from AGN is believed to originate from the cores of kiloparsec-scale jets of distant galaxies. Therefore AGN are not expected to be spatially resolvable by the LAT and provide a good calibration source to demonstrate that our extension detection method does not misidentify point-like sources as being extended. We note that megaparsec-scale  $\gamma$ -ray halos around AGNs have been hypothesized to be resolvable by the LAT (Aharonian et al. 1994). However, no such halo has been discovered in the LAT data so far.

Following 2FGL, the LAT Collaboration published the Second LAT AGN Catalog (2LAC), a list of high latitude ( $|b| > 10^\circ$ ) sources that had a high probability association with AGN (Ackermann et al. 2011). 2LAC associated 1016 2FGL sources with AGN. To avoid systematic problems with AGN classification, we selected only the 885 AGN which made it into the clean AGN sub-sample. An AGN association is considered clean only if it has a high probability of association  $P \geq 80\%$ , if it is the only AGN associated with the catalog source, and if there are no flags on the source in 2FGL. These last two conditions are important for our analysis. Source confusion may look like a spatially extended source and flagged catalog sources may correlate with unmodeled structure in the diffuse emission.

Of the 885 clean AGN, we selected the 783 of these 2FGL sources which were significantly-detected above 1 GeV and fit each of them for extension. The cumulative density of  $\text{TS}_{\text{ext}}$  for these AGN compared to the  $\chi^2_1/2$  distribution of Equation 8 is shown in Figure 9. The  $\text{TS}_{\text{ext}}$  distribution for AGN shows good agreement with the theoretical distribution, but two sources had  $\text{TS}_{\text{ext}} > 10$ . One was due to the incorrect removal of a nearby catalog sources from the sky model (see Section 9) and the other was due to a failure of convergence of the point-like source hypothesis. This result demonstrates that we can use  $\text{TS}_{\text{ext}}$  as a measure of the statistical significance of the detection of the extension of a source.

We should clarify that the LAT PSF used in this study was determined empirically by fitting the observed shape of bright AGN (see Section 8). Finding that the AGN we test are not extended is not surprising. This validation analysis is not suitable to reject any hypotheses about the existence of megaparsec-scale halos around AGN.

## 7. Analysis of Extended Sources Identified in 2FGL

**As further validation of our extended source method for studying spatially extended sources, we reanalyzed the twelve spatially extended sources which were included in 2FGL (Abdo et al. 2011d). Even though each of these sources required a dedicated analysis and they were fit with a variety of spatial models, it is valuable to show that these sources are significantly extended using our systematic extension method that assumed a radially-symmetric uniform surface brightness profile. On the other hand, for some of these sources a uniform disk spatial model does not well describe the observed extended emission and so the dedicated LAT publications provides a qualitatively better model these sources.**

Six extended SNRs were included in 2FGL: W51C, IC443, W28, W30, W44, the Cygnus Loop, and W30 (Abdo et al. 2009b, 2010i,e,h; Katagiri et al. 2011; Abdo et al. 2011c). Using

photons with energies between 1 GeV and 100 GeV, our analysis significantly detected the extension of all six of these SNRs.

Two nearby satellite galaxies of the Milky Way the Large Magellanic Cloud (LMC) and the Small Magellanic Cloud (SMC) were included in 2FGL as spatially extended sources (Abdo et al. 2010j,b). They were significantly detected using photons with energies between 1 GeV and 100 GeV. Our fit extension is comparable to the published result, but we note that the previous LAT Collaboration publication on LMC used a more complicated two 2D Gaussian surface brightness profile when fitting it ((Abdo et al. 2010j)).

Three PWNe, MSH 15–52, Vela X, and HESS J1825–137 were identified in 2FGL (Abdo et al. 2010a,f; Grondin et al. 2011). HESS J1825–137 was significantly detected using photons with energies between 10 GeV and 100 GeV. To improve our analysis of this source, we had to remove from our background model 2FGL J1823.1–1338c which was included in 2FGL to represent part of the extended emission. To avoid confusion with the nearby bright pulsar PSR J1509–5850, MSH 15–52 had to be analyzed at high energies. Using photons with energies above 10 GeV, we fit the extension of MSH 15–52 to be consistent with the published size but with an extension significance of  $TS_{\text{ext}} = 6.5$ .

Our analysis was unable to resolve Vela X which would have required first removing the pulsed photons from the Vela pulsar which was beyond the scope of this paper. Our analysis also failed to detect a significant extension for the Centaurus A Lobes because the source’s emission is significantly different from a uniform radially-symmetric surface brightness profile (Abdo et al. 2010c).

Our analysis of these sources is summarized in Table 3. This table includes the best fit position and extension of these sources when fitting them with a radially-symmetric uniform surface brightness profile. It also includes the best fit spectral parameters for each source. The position and extension of Vela X and the Centaurus A Lobes were taken from Abdo et al. (2010f,c) and are included in this list for completeness.

## 8. Systematic Errors on Extension

**For the extended sources presented in this paper, we developed two criteria for estimating systematic errors on the extension of the sources. First, we estimated a systematic error due to uncertainty in our knowledge of the LAT PSF.** Before launch, the LAT PSF was determined by detector simulations which were verified in accelerator tests (Atwood et al. 2009). However, in-flight data revealed a discrepancy above a few GeV in the PSF compared to the angular distribution of photons from bright AGN



(Abdo et al. 2011a). Subsequently, the PSF was fit empirically to bright AGN and this empirical parameterization is used in the P7\_V6 IRFs. To account for our uncertainty in our knowledge of the PSF, we refit our extended source candidates using the pre-flight Monte Carlo representation of the PSF and consider the difference in extension found using the two PSFs as a systematic error on the extension of a source. The same approach was used in Abdo et al. (2010i). At high energies, we believe that our parameterization of the PSF from bright AGN is substantially better than the Monte Carlo representation of the PSF so this systematic error is conservative.

**We estimated a second systematic error on the extension of a source due to uncertainty in our model of the Galactic diffuse emission by using an alternative model which takes as input templates calculated by GALPROP<sup>4</sup> but then fits each template locally in the surrounding region. The particular GALPROP model that was used as input is described in the LAT analysis of the isotropic diffuse emission (Abdo et al. 2010k).** The intensities of various components of the Galactic diffuse emission were fitted individually using a spatial distribution of the intensities within the ROI as predicted by the model. We distinguished contributions from CR interactions with the molecular hydrogen, the atomic+ionized hydrogen, residual gas traced by dust (Grenier et al. 2005), and the interstellar radiation field. We further split the contributions from interactions with molecular and atomic hydrogen to the Galactic diffuse emission according to the distance from the Galactic center in which they are produced. Hence, we replaced the standard diffuse emission model by 18 individually fitted templates to describe individual components of the diffuse emission. A similar crosscheck was used in the LAT Collaboration’s analysis of RX J1713.7–3946 (Abdo et al. 2011e).

**It is not expected that this diffuse model is superior to the standard LAT model obtained through an all-sky fit. However, adding degrees of freedom to the background model can remove likely spurious sources that correlate with features in the Galactic diffuse emission. Therefore, this tests systematics that may be due to imperfect modeling of the diffuse emission in the region. Nevertheless, this alternative diffuse model does not test all systematics related to the diffuse emission model. In particular, because the alternate model uses the same underlying gas maps it is unable to assess systematics due to mischaracterization of local diffuse structure due to lack of resolution of the underlying maps.**

---

<sup>4</sup>GALPROP is a software package for calculating the Galactic  $\gamma$ -ray emission based on a model of cosmic-ray propagation in the Galaxy (Strong & Moskalenko 1998; Vladimirov et al. 2011). See also <http://galprop.stanford.edu/> for details.

We do not expect the systematic error due to uncertainties in the PSF to be correlated with the systematic error due to uncertainty in the Galactic diffuse emission. Therefore, the total systematic error on the extension of a source was obtained by adding the two errors in quadrature.

## 9. Extended Source Search Method

Now that we have demonstrated that we understand the statistical issues associated with analyzing spatially extended sources (Section 3 and 6) and that our method can correctly analyze the extended sources included in 2FGL (Section 7), we apply this method to search for new spatially extended GeV sources.

Ideally, we would apply a completely blind and uniform search that tests the extension of each catalog source in the presence of all other 2FGL sources to find a complete list of all spatially extended sources. As our test of AGN in Section 6 showed, at high galactic latitude where the source density is not as great and the diffuse emission is less structured, this method works well.

But this is infeasible in the galactic plane where we most likely expect to discover new spatially extended sources. In the galactic plane, this analysis is challenged by our imperfect model of the diffuse emission and by issues related to source confusion. The Monte Carlo study in Section 5 showed that the overall likelihood would greatly increase when fitting a spatially extended source as two point-like sources so we expect that spatially extended LAT sources are modeled in 2FGL as multiple point-like sources. Furthermore, the position of other nearby sources in the region near an extended source could be biased by not correctly modeling the sources’ extension. Furthermore, 2FGL produced a list of sources significant at energies above 100 MeV whereas we are most sensitive to spatial extension at higher energies. Therefore, we expect that at higher energies our analysis would be complicated by 2FGL sources no longer significant and by 2FGL sources whose position was biased by diffuse emission at lower energies.

To account for these issues, we first produce a large list of possibly extended sources employing a very liberal search criteria and then refined the analysis of the promising candidates on a case by case basis. Our strategy tested all point-like 2FGL sources for extension assuming they had a uniform radially-symmetric uniform surface brightness profile and a power-law spectral model. Although not all extended sources are expected to have a shape very similar to

a uniform surface brightness profile, Section 2.4 showed that for many spatially extended sources the wide PSF of the LAT and limited statistics makes this a reasonable approximation. Additionally, our Monte Carlo study and AGN validation (Sections 3 and 6) demonstrate that we can use this shape for a statistically rigorous test. Because this spatial model only adds one additional degree of freedom, this test should be very sensitive. On the other hand, choosing this spatial model could bias us against finding extended sources that are not well described by uniform emission such as shell-type supernova remnants.

Before testing for extension, we automatically removed from the background model all other 2FGL sources within  $0.5^\circ$  of the source. This distance is somewhat arbitrary, but was picked in hopes of finding extended sources with sizes on the order of  $\sim 1^\circ$  or smaller. On the other hand, by removing these nearby background sources we expect to also incorrectly flag in our preliminary list point-like sources that are confused with nearby sources. To screen out obvious cases of source confusion, we performed the dual localization procedure described in Section 5 to compare the extended source hypothesis to the hypothesis of two independent point-like sources.

As was shown in Section 4, we gain little in sensitivity using photons with energies below 1 GeV. On the other hand, the large PSF at low energy makes us more susceptible to systematic errors arising from source confusion due to nearby soft point-like sources and by uncertainties in our modeling of the Galactic diffuse emission. In addition, the Galactic diffuse emission is more pronounced at lower energies due to its steep energy spectrum compared to the typical spectrum of extended sources (Abdo et al. 2009a). For that reason, we performed our search using only photons with energies between 1 GeV and 100 GeV.

We also performed a second search for extended sources using only photons with energies between 10 GeV and 100 GeV. Although this approach tests the same sources, it is complementary because the Galactic diffuse emission is even less dominant above 10 GeV. Furthermore, source confusion is less of a problem since many LAT sources are not significantly detected at energies exclusively above 10 GeV. Therefore, we expected to be able to resolve harder sources in more complicated regions by restricting our analysis to higher energies. The  $> 10$  GeV analysis is especially beneficial for regions near pulsars which are not significantly detected above 10 GeV. A similar procedure was used to detect the spatial extension of HESS J1825–137 and MSH 15–52 with the LAT (Abdo et al. 2010a; Grondin et al. 2011).

When we applied this test to the 1861 point-like sources in 2FGL, our search found 117 extended source candidates in the 1 GeV to 100 GeV energy range and 11 extended source candidates in the 10 GeV to 100 GeV energy range. Most of the extended sources flagged above 10 GeV were also flagged above 1 GeV. Many of these situations represent multiple point-like 2FGL sources all fitting the same emission region. For example, the sources 2FGL J1630.2-4752, 2FGL J1632.4-4753c, 2FGL J1634.4-4743c, and 2FGL J1636.3-4740c were all found to be spatially extended in the 10 GeV to 100 GeV energy range even though they all fit to similar positions and sizes. For these situations, we manually discarded all but one of the 2FGL sources.

Similarly, many of these sources were confused with nearby point-like sources or influence by large-scale residuals in the diffuse emission. To help determine which of these fits represented truly extended sources and in which of these fits the extension was influenced by source confusion and diffuse emission, we generated a series of diagnostic plots. For each candidate, we generated a map of the residual test statistic by adding a new source of spectral index 2 into the region at each position and finding the increase in likelihood when fitting its flux. Figure 10 shows this map around the most significantly extended source IC443 when it is modeled both as a point-like source and an extended source. The residual test statistic map indicates that the spatially extended model for IC443 is a significantly better description of the observed photons and that there is not significant residual in region after modeling the source as being spatially extended. We also generated maps of the sum of all counts within a given distance of the source and compared it to the model predictions assuming the emission originated from a point-like source. An example radial integral plot is shown for the extended source IC443 in Figure 1. For each source, we also made diffuse-emission-subtracted smoothed counts maps (show for IC443 in Figure 1).

It was very clear by visual inspection that in many cases our analysis was strongly influenced by large-scale residual in the diffuse emission and hence the extension measure was unreliable. This was especially true in our analysis of sources in the 1 GeV to 100 GeV energy range. An example of such a case is 2FGL J1856.2+0450c analyzed in the 1 GeV to 100 GeV energy range. Figure 11 shows a diffuse-emission-subtracted smoothed counts map around this source with the best fit extension of the source overlaid. There appears to be large-scale residual in the diffuse emission in this region along the Galactic plane. As a result, 2FGL J1856.2+0450c is fit to an extension of  $\sim 2^\circ$  and the result is statistically significant with  $\text{TS}_{\text{ext}} = 45.4$ . However, by looking at the residuals it

is clear that this complicated region is not well modeled. We manually discard sources like this.

Because of these systematic issues, we only selected extended source candidates in regions that did not appear dominated by these issues and in regions where there was an obvious spatially extended multiwavelength counterpart. Because of these systematic issues, this search can not be expected to be complete and it is likely that there are other spatially extended sources that this method missed.

For each candidate that was not biased by neighboring point-like sources or by large-scale residuals in the diffuse emission model, we improved the model of the region by decided on a case by case basis which background point-like sources should be kept. We kept sources that we believed represented physically distinct sources and we removed from the model of the sky sources that we believed were included in 2FGL to account for residual induced by not modeling the extension of the source and sources include in 2FGL to represent soft point-like sources that were not significant at higher energies. When deciding which background sources to keep and which to remove, we used as much as possible multiwavelength information about possibly extended source counterparts to help guide our choice. For each extended source presented in Section 10, we will describe any modification from 2FGL of the background model that were required.

The best fit position of nearby point-like sources can be influenced by the spatial model of a nearby extended source and vice versa. Similarly, the best fit position of nearby point-like sources in 2FGL can be biased by systematic errors at lower energies. Therefore, after selecting the list of background sources, we iteratively refit the position and spectrum of nearby background sources as well as the position and extension of the analyzed spatially extended sources until the overall fit globally converged. For each extended source, we will describe the position of any relocalized background sources.

After obtaining the overall best fit positions and extensions of all of the sources in the region using pointlike, we refit the spectral parameters of the region using gtlike. Using gtlike, we obtained a second measure of  $TS_{\text{ext}}$ . We only consider a source to be extended when both pointlike and gtlike agree that  $TS_{\text{ext}} > 16$ . We further required that  $TS_{\text{ext}} > 16$  using the alternate diffuse model presented in section 8. We then replaced the spatially extended source with two point-like sources and refit the position and spectrum of the

two point-like sources to calculate  $TS_{2pts}$ . We only consider a source to be spatially extended, instead of being the result of confusion of two point-like sources, if  $TS_{ext} > TS_{2pts}$ . As was shown in Section 5, this test is fairly powerful at removing situations in which the emission actually originates from two distinct point-like sources instead of one spatially extended source. On the other hand, it is still possible that improved observations could resolve additional structure or new sources that we are currently not sensitive to. Considering the very complicated morphologies of extended sources observed at other wavelengths and the high density of possible sources that are expected to emit at GeV energies, it is likely that in some of these regions further observations will resolve that the emission is significantly more complicated than the simple radially-symmetric uniform surface brightness profile that we assume.

## 10. New Extended Sources

Nine extended sources not included in 2FGL were found by our extended source search. Two of these have been previously studied in dedicated publications: RXJ1713.7–3946 and Vela Jr. (Abdo et al. 2011e,b). Three of these sources were found when using photons with energies between 1 GeV and 100 GeV and six were found when using photons with energies between 10 GeV and 100 GeV. For the sources found at energies above 10 GeV, we restrict our analysis to higher energies because of the issues of source confusion and diffuse emission modeling described in section 9. The spectral and spatial properties of these nine sources is summarized in Table 4 and the results of our investigation of systematic errors are presented in Table 5. Table 5 also compares the likelihood assuming the source is spatially extended to the likelihood assuming that the emission originates from two independent point-like sources. For these new extended sources,  $TS_{ext} > TS_{2pts}$  so we conclude that the GeV emission does not originate from two physically distinct point-like sources (see Section 5). Table 5 also includes the results of the extension fit using variations of the PSF and the galactic diffuse model described in Section 8. There is good agreement between  $TS_{ext}$  and the fit size using the standard analysis, the alternative diffuse models, and the alternative PSF. This suggests that the sources are robust against features in the diffuse emission model and uncertainties in the angular resolution of the LAT.

### 10.1. 2FGL J0823.0–4246

2FGL J0823.0–4246 was found by our search to be an extended source candidate in the 10 GeV to 100 GeV energy range and is spatially coincident with the SNR Puppis A. Figure 12 shows a counts map of this source and overlays and *ROSAT* X-ray contours of Puppis A. There are two nearby catalog sources 2FGL J0823.4–4305 and 2FGL J0821.0–4254 that are also coincident with the SNR but that do not appear to represent physically distinct sources. We concluded that these nearby point-like sources were included in 2FGL to account for residual induced by not modeling the extension of this source and removed them from our model of the sky. After removing these sources, 2FGL J0823.0–4246 was found to have an extension of  $0^\circ 37 \pm 0^\circ 03_{\text{stat}} \pm 0^\circ 02_{\text{sys}}$  with an extension significance of  $\text{TS}_{\text{ext}} = 46.3$ . Figure 13 shows the spectrum of this source.

Puppis A has been studied in detail in radio (Castelletti et al. (2006), and references therein) and X-ray (Petre et al. (1996); Hwang et al. (2008), and references therein). The fit extension of 2FGL J0823.0–4246 matches well its inferred size at GeV energies. Puppis A’s distance was estimated at 2.2 kpc (Reynoso et al. 1995, 2003) and leads to a 1 GeV to 100 GeV luminosity of  $\sim 3 \times 10^{34} \text{ ergs s}^{-1}$ . No molecular clouds have been observed directly adjacent to Puppis A (Paron et al. 2008), similar to the LAT detected Cyngus Loop SNR (Katagiri et al. 2011). The luminosity of Puppis A is also smaller than that of other SNRs believed to interact with molecular clouds (Abdo et al. 2009b, 2010i,h,e,g).

### 10.2. 2FGL J1627.0–2425c

2FGL J1627.0–2425c was found by our search to have an extension of  $0^\circ 41 \pm 0^\circ 05_{\text{stat}} \pm 0^\circ 02_{\text{sys}}$  with an extension significance of  $\text{TS}_{\text{ext}} = 31.1$  using photons with energies between 1 GeV and 100 GeV. The source Figure 14 shows a counts map of this source.

This source is in a region of remarkably complicated diffuse emission. Even though it is  $16^\circ$  from the Galactic plane, this source is on top of the core of the Ophiuchus molecular cloud which contains massive star-forming regions that are bright in the infrared. The region also has abundant molecular and atomic gas traced by CO and HI but also plenty of dark gas found only by its association with dust emission (Grenier et al. 2005). Embedded star-forming regions make it even more challenging to measure the column density of dust. Infrared and  $^{12}\text{CO}$  ( $J = 1 \rightarrow 0$ ) contours are overlaid on Figure 14 and show good spatial correlation



with the GeV emission (Young et al. 1986; de Geus et al. 1990). This source might represent  $\gamma$ -ray emission from the interactions of cosmic rays with interstellar gas which has not been accounted for in the LAT diffuse emission model.

### 10.3. 2FGL J1712.4–3941

2FGL J1712.4–3941 was found by our search to be spatially extended using photons with energies between 1 GeV and 100 GeV. This source is spatially coincident with the SNR RX J1713.7–3946 and was recently studied by the LAT collaboration in Abdo et al. (2011e). Figure 15a shows a smoothed counts map of the source and overlays TeV contours of the SNR Aharonian et al. (2007b). To analyze this source, we used the same background source model as the recent LAT publication. Figure 15b shows the source after subtracting these background sources. With this background, RX J1713.7–3946 fit to an extension of  $0^\circ.56 \pm 0^\circ.04_{\text{stat}} \pm 0^\circ.02_{\text{sys}}$  with an extension significance of  $\text{TS}_{\text{ext}} = 39.6$ .

### 10.4. 2FGL J0851.7–4635

2FGL J0851.7–4635 was found by our search to be an extended source candidate in the 10 GeV to 100 GeV energy range and is spatially coincident with the SNR Vela Jr. This source was recently studied by the LAT collaboration in Abdo et al. (2011b). Figure 16 shows a counts map of the source. Overlaid on Figure 16 are TeV contours of Vela Jr. (Aharonian et al. 2007a). There are three point-like catalog sources 2FGL J0853.5–4711, 2FGL J0848.5–4535, and 2FGL J0855.4–4625 which correlate with the multiwavelength emission of this SNR but do not appear to be physically distinct sources. They were most likely included in 2FGL to account for residual induced by not modeling the extension Vela Jr. and were removed from our model of the sky. In addition, two further away sources 2FGL J0858.0–4815 and 2FGL J0901.7–4655 were removed from our model of the sky because they were not significant above 10 GeV.

With this model of the background, 2FGL J0851.7–4635 was found to have an extension of  $1^\circ.13 \pm 0^\circ.08_{\text{stat}} \pm 0^\circ.05_{\text{sys}}$  with an extension significance of  $\text{TS}_{\text{ext}} = 87.2$ . The LAT size matches well the TeV morphology of Vela Jr. While fitting the extension of 2FGL J0851.7–4635, we iteratively relocalized the position of the nearby point-like catalog source 2FGL J0854.7–4501 to  $(l, b) = (266^\circ.24, 0^\circ.49)$  to

better fit its position at high energies.

## 10.5. 2FGL J1615.0–5051

2FGL J1615.0–5051 and 2FGL J1615.2–5138 were both found to be extended source candidates in the 10 GeV to 100 GeV energy range. They are less than  $1^\circ$  away from each other and needed to be analyzed simultaneously. 2FGL J1615.0–5051 is spatially coincident with the extended TeV source HESS J1616–508 and 2FGL J1615.2–5138 is coincident with the extended TeV source HESS J1614–518. Figure 17 shows a counts map of these sources and overlays the TeV contours of HESS J1616–508 and HESS J1614–518 (Aharonian et al. 2006). The figure shows that the 2FGL source 2FGL J1614.9–5212 is very close to 2FGL J1615.2–5138 and correlates with the same extended TeV source as 2FGL J1615.2–5138. We concluded that this source was included in 2FGL to account for residual induced by not modeling the extension of 2FGL J1615.2–5138 and removed it from our model of the sky. There are two further away sources 2FGL J1619.7–5040c and 2FGL J1620.6–5111c that were removed from our model because they were not significant at energies above 10 GeV.

With this model of the sky, we iteratively fit the extensions of 2FGL J1615.0–5051 and 2FGL J1615.2–5138. 2FGL J1615.0–5051 was found to have an extension of  $0^\circ 33 \pm 0^\circ 04_{\text{stat}} \pm 0^\circ 01_{\text{sys}}$  with an extension significance of  $\text{TS}_{\text{ext}} = 16.3$ . 2FGL J1615.2–5138 was found to have an extension of  $0^\circ 42 \pm 0^\circ 03_{\text{stat}} \pm 0^\circ 01_{\text{sys}}$  with an extension significance of  $\text{TS}_{\text{ext}} = 48.0$ . To test for the possibility that 2FGL J1615.2–5138 is not spatially extended but instead composed of two point-like sources (one of them reprinted in 2FGL by 2FGL J1614.9–5212), we refit 2FGL J1615.2–5138 as two point-like sources. Because  $\text{TS}_{2\text{pts}}$  is less than  $\text{TS}_{\text{ext}}$ , we conclude that this emission does not originate from two nearby point-like sources.

2FGL J1615.0–5051’s TeV counterpart HESS J1616–508’s was fit with a radially-symmetric Gaussian surface brightness profile to have an extension  $0^\circ 136 \pm 0^\circ 008$ . This TeV size corresponds to a 68% containment radius of  $r_{68} = 0^\circ 21 \pm 0^\circ 01$ , comparable to the LAT size  $r_{68} = 0^\circ 27 \pm 0^\circ 03$ . Figure 18 shows that the spectrum of 2FGL J1615.0–5051 at GeV energies connects to the spectrum of HESS J1616–508 at TeV energies.

HESS J1616–508 is located in the region of two SNRs RCW103 (G332.4–04) and Kes 32 (G332.4+0.1) but is not spatially coincident with either of them

(Aharonian et al. 2006). HESS J1616–508 is near three pulsars PSR J1614–5048, PSR J1616–5109, and PSR J1617–5055. (Torii et al. 1998; Landi et al. 2007a). Only PSR J1617–5055 is energetically capable of powering the TeV emission and Aharonian et al. (2006) speculated that HESS J1616–508 could be a PWN powered by this young pulsar. Because HESS J1616–508 is  $9'$  away from PSR J1617–5055, this would require an asymmetric X-ray PWNe to power the TeV emission. *Chandra* ACIS observations revealed an underluminous PWN of size  $\sim 1'$  around the pulsar that was not oriented towards the TeV emission rendering this association uncertain (Kargaltsev et al. 2009). No other promising counterparts were observed at X-ray and soft gamma-ray energies by *Suzaku* (Matsumoto et al. 2007), *Swift*/XRT, IBIS/ISGRBI, BeppoSAX and *XMM-Newton* (Landi et al. 2007a). Kargaltsev et al. (2009) discovered some additional diffuse emission towards the center of HESS J1616–508 using archival radio and infrared observations. Deeper observations will likely be necessary to understand this  $\gamma$ -ray source.

## 10.6. 2FGL J1615.2–5138

2FGL J1615.2–5138 is spatially coincident with the extended TeV source HESS J1614–518. H.E.S.S. measured a 2D Gaussian extension of  $\sigma = 0^\circ.23 \pm 0^\circ.02$  and  $\sigma = 0^\circ.15 \pm 0^\circ.02$  in the semi-major and semi-minor axis. This corresponds to a 68% containment size of  $r_{68} = 0^\circ.35 \pm 0^\circ.03$  and  $0^\circ.23 \pm 0^\circ.03$ , consistent with the LAT size  $r_{68} = 0^\circ.35 \pm 0^\circ.03$ . Figure 18 shows that the spectrum of 2FGL J1615.2–5138 at GeV energies connects to the spectrum of HESS J1614–518 at TeV energies. Further data collected by H.E.S.S. in 2007 resolve a double peaked structure at TeV energies but no spectral variation across this source, suggesting that the emission is not the confusion of physically separate sources (Rowell et al. 2008). This double peaked structure is also hinted at in the LAT counts map in Figure 17 but is not very significant. The TeV source was also detected by CANGAROO-III (Mizukami et al. 2011).

There are five nearby pulsars, but none are luminous enough to provide the energy output required to power the  $\gamma$ -ray emission (Rowell et al. 2008). HESS J1614–518 is spatially coincident with a young open cluster Pismis 22 (Landi et al. 2007b; Rowell et al. 2008). *Suzaku* detected two promising X-ray candidates. Source A is an extended source consistent with the peak of HESS J1614–518 and source B coincident with Pismis 22 and towards the cen-

ter but in a relatively dim region of HESS J1614–518 (Matsumoto et al. 2008). Three hypothesis have been presented to explain this emission; either source A is an SNR powering the  $\gamma$ -ray emission, source A is a PWN powered by an undiscovered pulsar in either source A or B, and finally that the emission may arise from hadronic acceleration in the stellar winds of Pisim 22 (Mizukami et al. 2011).

### 10.7. 2FGL J1632.4–4753c

2FGL J1632.4–4753c was found by our search to be an extended source candidate in the 10 GeV to 100 GeV energy range but is in a crowded region of the sky. It is spatially coincident with the TeV source HESS J1632–478. Figure 19a shows a counts map of this source and overlays TeV contours of HESS J1632–478 (Aharonian et al. 2006). The figure shows that there are three nearby point-like 2FGL sources 2FGL J1631.7–4720c, 2FGL J1630.2–4752, 2FGL J1634.4–4743c that correlate with the extended TeV source but that do appear to be physically distinct sources. We concluded that they were included in 2FGL to account for residual induced by not modeling the extension of 2FGL J1632.4–4753c and removed them from our model of the sky. We also removed four farther away sources 2FGL J1638.0–4703c, 2FGL J1628.1–4857c, 2FGL J1630.1–4615, 2FGL J1639.8–4921c because they were not significant above 10 GeV.

Our sky model therefore included three nearby sources 2FGL J1632.4–4820c, 2FGL J1635.4–4717c, 2FGL J1636.3–4740c and which do not correlate with the extended TeV emission of HESS J1632–478 as well as the extended source candidate 2FGL J1632.4–4753c. Figure 19b shows the same region with these background sources subtracted. With this model, 2FGL J1632.4–4753c was found to have an extension of  $0^\circ.44 \pm 0^\circ.04_{\text{stat}} \pm 0^\circ.03_{\text{sys}}$  with an extension significance of  $\text{TS}_{\text{ext}} = 64.5$ . While fitting the extension of 2FGL J1632.4–4753c, we iteratively relocalized 2FGL J1635.4–4717c to  $(l, b) = (337^\circ.23, 0^\circ.35)$  and 2FGL J1636.3–4740c to  $(l, b) = (336^\circ.97, -0^\circ.07)$ .

H.E.S.S. measured a extension of  $\sigma = 0^\circ.21 \pm 0^\circ.05$  and  $0^\circ.06 \pm 0^\circ.04$  along the semi-major and semi-minor axes when fitting HESS J1632–478 with an elliptical 2D Gaussian surface brightness profile. This corresponds to a 68% containment size  $r_{68} = 0^\circ.31 \pm 0^\circ.08$  and  $0^\circ.09 \pm 0^\circ.06$  along the semi-major and semi-minor axis, consistent with the LAT size  $r_{68} = 0^\circ.36 \pm 0^\circ.04$ . Figure 18 shows that the spectrum of 2FGL J1632.4–4753c at GeV energies connects to the spectrum of

HESS J1632–478 at TeV energies.

Aharonian et al. (2006) argued that HESS J1632–478 is positionally coincident with the hard X-ray source IGR J1632–4751 observed by *ASCA*, *INTEGRAL*, and *XMM-Newton* (Sugizaki et al. 2001; Tomsick et al. 2003; Rodriguez et al. 2003), but this source is suspected to be a galactic X-Ray Binary so the  $\gamma$ -ray extension disfavors the association. Further observations by *XMM-Newton* discovered point-like emission coincident with the peak of the H.E.S.S. source surrounded by extended emission of size  $\sim 32'' \times 15''$  (Balbo et al. 2010). They found in archival MGPS-2 data a spatially coincident extended radio source (Murphy et al. 2007) and argued for a single synchrotron process producing the radio, X-ray, and TeV emission, likely due to a PWNe. The increased size at TeV energies compared to X-ray energies has previously been observed in several aging PWNe including HESS J1825–137 (Gaensler et al. 2003; Aharonian et al. 2006b), HESS J1640–465 (Aharonian et al. 2006; Funk et al. 2007), and Vela X (Markwardt & Ogelman 1995; Aharonian et al. 2006c) and can be explained by different synchrotron cooling times for the electrons that produce X-rays and  $\gamma$ -rays.

## 10.8. 2FGL J1837.3–0700c

2FGL J1837.3–0700c was found by our search to be an extended source candidate in the 10 GeV to 100 GeV energy range and is spatially coincident with the TeV source HESS J1837–069. This source is in a complicated region. Figure 20a shows a smoothed counts map of the region and overlays the TeV contours of HESS J1837–069 (Aharonian et al. 2006). There are two very nearby point-like 2FGL sources 2FGL J1836.8–0623c, and 2FGL J1839.3–0558c that clearly represent distinct sources. On the other hand, there is another source 2FGL J1835.5–0649 located between the three sources that appears to correlate with the TeV morphology of HESS J1837–069 but does not appear to represent a physically distinct source. We concluded that this source was included in 2FGL to account for residual induced by not modeling the extension of this source and removed it from our model of the sky. We also removed from our model of the sky the farther away point-like 2FGL source 2FGL J1839.0–0539 because it was not significant with energies above 10 GeV. Figure 20b shows a counts map of this region after subtracted these background sources.

With this model, 2FGL J1837.3–0700c was found to have an extension of

0°35 ± 0°08<sub>stat</sub> ± 0°03<sub>sys</sub> with an extension significance of  $TS_{\text{ext}} = 18.8$ . While fitting the extension of 2FGL J1837.3–0700c, we iteratively relocalized the three nearest background sources along with the extension of 2FGL J1837.3–0700c but their positions did not significantly change. 2FGL J1834.7–0705c moved to  $(l, b) = (24^\circ 77', 0^\circ 50')$ , 2FGL J1836.8–0623c moved to  $(l, b) = (25^\circ 57', 0^\circ 32')$ , and 2FGL J1839.3–0558c moved to  $(l, b) = (26^\circ 08', 0^\circ 23')$ . With this best fit sky model, we tested for source confusion by fitting the source instead as two point-like sources. Because  $TS_{2\text{pts}}$  is less than  $TS_{\text{ext}}$ , we concluded that this emission does not originate from two nearby point-like sources.

H.E.S.S. measured an extension of  $\sigma = 0^\circ 12 \pm 0^\circ 02$  and  $0^\circ 05 \pm 0^\circ 02$  of the coincident TeV source HESS J1837–069 along the semi-major and semi-minor axis when fitting this source with an elliptical 2D Gaussian surface brightness profile. This corresponds to a 68% containment radius of  $r_{68} = 0^\circ 18 \pm 0^\circ 03$  and  $0^\circ 08 \pm 0^\circ 03$  along the semi-major and semi-minor axis. The size is not significantly different from the LAT 68% containment radius of  $r_{68} = 0^\circ 29 \pm 0^\circ 07$  (less than  $2\sigma$ ). Figure 18 shows that the spectrum of 2FGL J1837.3–0700c at GeV energies connects to the spectrum of HESS J1837–069 at TeV energies.

HESS J1837–069 is coincident with the hard and steady X-ray source AX J1838.0–0655 (Bamba et al. 2003). This source was discovered by RXTE to be a pulsar sufficiently luminous to power the TeV emission and was resolved by *Chandra* to be a bright point-like source surrounded by a  $\sim 2'$  nebula (Gotthelf & Halpern 2008). The  $\gamma$ -ray emission may be powered by this pulsar. 2FGL J1837.3–0700c’s hard spectral index and spatial extension disfavor a pulsar origin of the LAT emission and suggest instead that the GeV and TeV emission both originate from the pulsar’s wind. There is another X-ray point-like source AX J1837.3–0652 near HESS J1837–069 (Bamba et al. 2003) that was also resolved into a point-like and diffuse component (Gotthelf & Halpern 2008). Although no pulsations have been detected from it, it could also be a pulsar powering some of the  $\gamma$ -ray emission.

## 10.9. 2FGL J2021.5+4026

The source 2FGL J2021.5+4026 is coincident with 2CG 078+01 and 3EG J2020+4017 (Swanenburg et al. 1981; Hartman et al. 1999) and also with the  $\gamma$ -Cygni SNR. This  $\gamma$ -ray source has been speculated to originate from the interaction of accelerated particles in the SNR with dense molecular clouds (Pollock 1985; Gaisser et al.

1998), but this association was disfavored when the LAT GeV emission from this source was detected to be pulsed (PSR J2021+4026, Abdo et al. (2010)). This pulsar was also been observed by AGILE (Chen et al. 2011).

Looking at the same region at energies above 10 GeV, the pulsar is no longer significant but we instead found in our search an extended source candidate. Figure 21 shows a counts map of this source and overlays radio contours of  $\gamma$ -Cygni from the Canadian Galactic Plane Survey (Taylor et al. 2003). There is good spatial overlap between the SNR and the GeV emission.

There is a nearby source 2FGL J2019.1+4040 that correlates with the radio emission of  $\gamma$ -Cygni and does not appear to represent a physically distinct source. We concluded that it was included in 2FGL to account for residual induced by not modeling the extension of  $\gamma$ -Cygni and removed it from our model of the sky. We also removed from our model of the sky the four farther away sources 2FGL J2022.8+3843c, 2FGL J2020.0+4159, 2FGL J2013.8+4115c, and 2FGL J2012.4+3955c because they were not significant when observed at energies above 10 GeV. Furthermore, we decided to add to our region an additional point-like source at  $(l, b) = (78^\circ 85, 2^\circ 67)$ . Although this source is not very significant ( $TS = 13.5$  in the 10 GeV to 100 GeV energy range), its location is outside the multiwavelength contours of  $\gamma$ -Cygni and modeling it improved the connection of the best fit extension with the multiwavelength contours of  $\gamma$ -Cygni. Nevertheless, the overall spatial and spectral characteristics of the source were not significantly changed by the presence of this source.

With this model, 2FGL J2021.5+4026 was found to have an extension of  $0^\circ 59 \pm 0^\circ 03_{\text{stat}} \pm 0^\circ 02_{\text{sys}}$  with an extension significance of  $TS_{\text{ext}} = 116.4$ . Figure 13 shows its spectrum. The inferred size of this source at GeV energies well matches the radio size of  $\gamma$ -Cygni. Milagro detected a  $4.2\sigma$  excess at energies  $\sim 30$  TeV from this location (Abdo et al. 2009c,d). Veritas also detected an extended source VER J2019+407 coincident with the SNR above 200 GeV and suggested that the TeV emission could be a shock-cloud interaction in  $\gamma$ -Cygni (Weinstein 2009).

## 11. Discussion

Twelve extended sources were included in 2FGL and two additional extended sources were studied in dedicated publications. Using two years of LAT data and



**a new analysis method, we presented the detection of seven additional extended sources.**

We also reanalyze the spatial shape of the twelve extended sources in 2FGL and the two additional sources. The 21 extended LAT sources are located primarily along the Galactic plane and their locations are shown in Figure 22. Most of the LAT detected extended sources are expected to be of Galactic origin as the distance of extragalactic sources (with the exception of the local group Galaxies) is typically too large to be able to resolve them at  $\gamma$ -rays energies.

For the LAT extended sources also seen at TeV energies, Figure 23 shows that there is a good correlation between the size of the sources at GeV and TeV energies. Even so, the size of PWNe are expected to vary across the GeV and TeV energy range and the size of HESS J1825–137 is significantly larger at GeV than TeV energies (Grondin et al. 2011). It is interesting to compare the size of other PWN candidates at GeV and TeV energies, but definitively measuring this would require a more in-depth analysis of the LAT data using the same elliptical surface brightness profile.

Figure 24 compares the size of the 21 extended LAT sources to the 42 extended H.E.S.S. sources.<sup>5</sup> Because of the large field of view and all-sky coverage, the LAT can more easily measure larger sources. On the other hand, the better angular resolution of air Cherenkov detectors allows them to measure a population of extended sources below our detection threshold limit (currently about  $\sim 0^\circ.2$ ). *Fermi* has a five year nominal mission lifetime with a goal of ten years of operation. As Figure 6 shows, the low background of the LAT at high energies allows its sensitivity to these smaller sources to improve by a factor greater than the square root of the exposure. With increasing exposure, the LAT will likely begin to detect and resolve some of these smaller TeV sources.

Figure 25 compares the spectral index of LAT detected extended sources and of all sources in 2FGL. This, and Table 3 and 4, show that the LAT observes a population of hard extended sources at energies above 10 GeV. Figure 18 shows that the spectra of four of these sources (2FGL J1615.0–5051, 2FGL J1615.2–5138, 2FGL J1632.4–4753c, and 2FGL J1837.3–0700c) at GeV energies connects to the spectra of their H.E.S.S. counterparts at TeV energies. This is also true of Vela Jr., HESS J1825–137 (Grondin et al. 2011), and RX J1713.7–3946 (Abdo et al. 2011e). It is likely that the GeV and TeV emission from these sources originates from the same population of high-energy particles.

Many of the TeV detected extended sources now seen at GeV energies are currently unidentified and further multiwavelength follow-up observations will be necessary to under-

---

<sup>5</sup>The TeV extension of the 42 extended H.E.S.S. sources comes from the H.E.S.S. Source Catalog. The H.E.S.S. source catalog can be found at <http://www.mpi-hd.mpg.de/hfm/HESS/pages/home/sources/>.

stand these particle accelerators. But the extension of the spectrum of these TeV sources towards lower energies by LAT observations can help to determine the origin and nature of the high-energy emission seen from these sources.

The *Fermi* LAT Collaboration acknowledges generous ongoing support from a number of agencies and institutes that have supported both the development and the operation of the LAT as well as scientific data analysis. These include the National Aeronautics and Space Administration and the Department of Energy in the United States, the Commissariat à l’Energie Atomique and the Centre National de la Recherche Scientifique / Institut National de Physique Nucléaire et de Physique des Particules in France, the Agenzia Spaziale Italiana and the Istituto Nazionale di Fisica Nucleare in Italy, the Ministry of Education, Culture, Sports, Science and Technology (MEXT), High Energy Accelerator Research Organization (KEK) and Japan Aerospace Exploration Agency (JAXA) in Japan, and the K. A. Wallenberg Foundation, the Swedish Research Council and the Swedish National Space Board in Sweden.

Additional support for science analysis during the operations phase is gratefully acknowledged from the Istituto Nazionale di Astrofisica in Italy and the Centre National d’Études Spatiales in France.

This research has made use of `pywcsgrid2`, an open-source plotting package for Python<sup>6</sup>. The authors acknowledge the use of `HEALPix`<sup>7</sup> (Górski et al. 2005).

## REFERENCES

- Abdo, A. A., et al. 2009a, Physical Review Letters, 103, 251101
- . 2009b, ApJ, 706, L1
- . 2009c, ApJS, 183, 46
- . 2009d, ApJ, 700, L127
- . 2009e, Astroparticle Physics, 32, 193
- . 2010a, ApJ, 714, 927

---

<sup>6</sup><http://leejjoon.github.com/pywcsgrid2/>

<sup>7</sup><http://healpix.jpl.nasa.gov/>

- 981 —. 2010b, A&A, 523, A46+
- 982 —. 2010c, Science, 328, 725
- 983 —. 2010d, ApJS, 188, 405
- 984 —. 2010e, ApJ, 718, 348
- 985 —. 2010f, ArXiv e-prints
- 986 —. 2010g, ArXiv e-prints
- 987 —. 2010h, Science, 327, 1103
- 988 —. 2010i, ApJ, 712, 459
- 989 —. 2010j, A&A
- 990 —. 2010k, Physical Review Letters, 104, 101101
- 991 —. 2010l, ApJS, 187, 460
- 992 —. 2011a, Astroparticle Physics, in preparation
- 993 —. 2011b, ApJ, in preparation
- 994 —. 2011c, ArXiv e-prints
- 995 —. 2011d, ArXiv e-prints
- 996 —. 2011e, ApJ, 734, 28
- 997 Acciari, V. A., et al. 2009, ApJ, 698, L133
- 998 —. 2011, ArXiv e-prints
- 999 Ackermann, M., et al. 2011, ArXiv e-prints
- 1000 Aharonian, F., et al. 2005, A&A, 435, L17
- 1001 —. 2006a, A&A, 460, 743
- 1002 —. 2006b, A&A, 460, 365
- 1003 —. 2006c, A&A, 448, L43
- 1004 Aharonian, F., et al. 2006, ApJ, 636, 777

- 1005 Aharonian, F., et al. 2007a, *ApJ*, 661, 236
- 1006 —. 2007b, *A&A*, 464, 235
- 1007 —. 2008, *A&A*, 481, 401
- 1008 Aharonian, F. A., Coppi, P. S., & Voelk, H. J. 1994, *ApJ*, 423, L5
- 1009 Aharonian, F. A., et al. 2007c, *A&A*, 469, L1
- 1010 Albert, J., et al. 2006, *Science*, 312, 1771
- 1011 Atwood, W. B., et al. 2009, *ApJ*, 697, 1071
- 1012 Balbo, M., Saouter, P., Walter, R., Pavan, L., Tramacere, A., Pohl, M., & Zurita-Heras,  
1013 J.-A. 2010, *A&A*, 520, A111+
- 1014 Baltz, E. A., et al. 2008, *J. Cosmology Astropart. Phys.*, 7, 13
- 1015 Bamba, A., Ueno, M., Koyama, K., & Yamauchi, S. 2003, *ApJ*, 589, 253
- 1016 Castelletti, G., Dubner, G., Golap, K., & Goss, W. M. 2006, *A&A*, 459, 535
- 1017 Chen, A. W., et al. 2011, *A&A*, 525, A33+
- 1018 Dame, T. M. 2011, *ArXiv e-prints*
- 1019 de Geus, E. J., Bronfman, L., & Thaddeus, P. 1990, *A&A*, 231, 137
- 1020 Eadie, W. T., Drijard, D., & James, F. E. 1971, *Statistical methods in experimental physics*,  
1021 ed. Eadie, W. T., Drijard, D., & James, F. E.
- 1022 Funk, S., Hinton, J. A., Pühlhofer, G., Aharonian, F. A., Hofmann, W., Reimer, O., &  
1023 Wagner, S. 2007, *ApJ*, 662, 517
- 1024 Gaensler, B. M., Schulz, N. S., Kaspi, V. M., Pivovarov, M. J., & Becker, W. E. 2003, *ApJ*,  
1025 588, 441
- 1026 Gaisser, T. K., Protheroe, R. J., & Stanev, T. 1998, *ApJ*, 492, 219
- 1027 Górski, K. M., Hivon, E., Banday, A. J., Wandelt, B. D., Hansen, F. K., Reinecke, M., &  
1028 Bartelmann, M. 2005, *ApJ*, 622, 759
- 1029 Gotthelf, E. V., & Halpern, J. P. 2008, *ApJ*, 681, 515
- 1030 Grenier, I. A., Casandjian, J.-M., & Terrier, R. 2005, *Science*, 307, 1292

- 1031 Grondin, M. ., et al. 2011, ArXiv e-prints
- 1032 Hartman, R. C., et al. 1999, ApJS, 123, 79
- 1033 Hwang, U., Petre, R., & Flanagan, K. A. 2008, ApJ, 676, 378
- 1034 James, F., & Roos, M. 1975, Comput. Phys. Commun., 10, 343
- 1035 Kargaltsev, O., Pavlov, G. G., & Wong, J. A. 2009, The Astrophysical Journal, 690, 891
- 1036 Katagiri, H., et al. 2011, ArXiv e-prints
- 1037 Kerr, M. 2011, PhD in physics, University of Washington
- 1038 King, I. 1962, AJ, 67, 471
- 1039 Krause, J., Carmona, E., & Reichardt, I. 2011, in (Presented at the 2011 Fermi Symposium,  
1040 Rome Italy)
- 1041 Landi, R., de Rosa, A., Dean, A. J., Bassani, L., Ubertini, P., & Bird, A. J. 2007a, MNRAS,  
1042 380, 926
- 1043 Landi, R., Masetti, N., Bassani, L., Cellone, S. A., Romero, G. E., Ubertini, P., & Dean,  
1044 A. J. 2007b, The Astronomer’s Telegram, 1047, 1
- 1045 Markwardt, C. B., & Ogelman, H. 1995, Nature, 375, 40
- 1046 Matsumoto, H., et al. 2007, PASJ, 59, 199
- 1047 —. 2008, PASJ, 60, 163
- 1048 Mattox, J. R., et al. 1996, ApJ, 461, 396
- 1049 Mizukami, T., et al. 2011, ArXiv e-prints
- 1050 Murphy, T., Mauch, T., Green, A., Hunstead, R. W., Piestrzynska, B., Kels, A. P., &  
1051 Sztajer, P. 2007, MNRAS, 382, 382
- 1052 Paron, S., Dubner, G., Reynoso, E., & Rubio, M. 2008, A&A, 480, 439
- 1053 Petre, R., Becker, C. M., & Winkler, P. F. 1996, ApJ, 465, L43+
- 1054 Pollock, A. M. T. 1985, A&A, 150, 339
- 1055 Protassov, R., van Dyk, D. A., Connors, A., Kashyap, V. L., & Siemiginowska, A. 2002,  
1056 ApJ, 571, 545

- 1057 Reynoso, E. M., Dubner, G. M., Goss, W. M., & Arnal, E. M. 1995, *AJ*, 110, 318
- 1058 Reynoso, E. M., Green, A. J., Johnston, S., Dubner, G. M., Giacani, E. B., & Goss, W. M.  
1059 2003, *MNRAS*, 345, 671
- 1060 Rodriguez, J., Tomsick, J. A., Foschini, L., Walter, R., Goldwurm, A., Corbel, S., & Kaaret,  
1061 P. 2003, *A&A*, 407, L41
- 1062 Rowell, G., Horns, D., Fukui, Y., & Moriguchi, Y. 2008, in *American Institute of Physics*  
1063 *Conference Series*, Vol. 1085, *American Institute of Physics Conference Series*, ed.  
1064 F. A. Aharonian, W. Hofmann, & F. Rieger, 241–244
- 1065 Sreekumar, P., et al. 1998, *The Astrophysical Journal*, 494, 523
- 1066 Strong, A. W., & Moskalenko, I. V. 1998, *ApJ*, 509, 212
- 1067 Sugizaki, M., Mitsuda, K., Kaneda, H., Matsuzaki, K., Yamauchi, S., & Koyama, K. 2001,  
1068 *ApJS*, 134, 77
- 1069 Swanenburg, B. N., et al. 1981, *ApJ*, 243, L69
- 1070 Taylor, A. R., et al. 2003, *AJ*, 125, 3145
- 1071 Tomsick, J. A., Lingenfelter, R., Walter, R., Rodriguez, J., Goldwurm, A., Corbel, S., &  
1072 Kaaret, P. 2003, *IAU Circ.*, 8076, 1
- 1073 Torii, K., et al. 1998, *ApJ*, 494, L207+
- 1074 Vladimirov, A. E., et al. 2011, *Computer Physics Communications*, 182, 1156
- 1075 Weekes, T. C., et al. 1989, *ApJ*, 342, 379
- 1076 Weinstein, A. 2009, *ArXiv e-prints*
- 1077 Young, E. T., Lada, C. J., & Wilking, B. A. 1986, *ApJ*, 304, L45

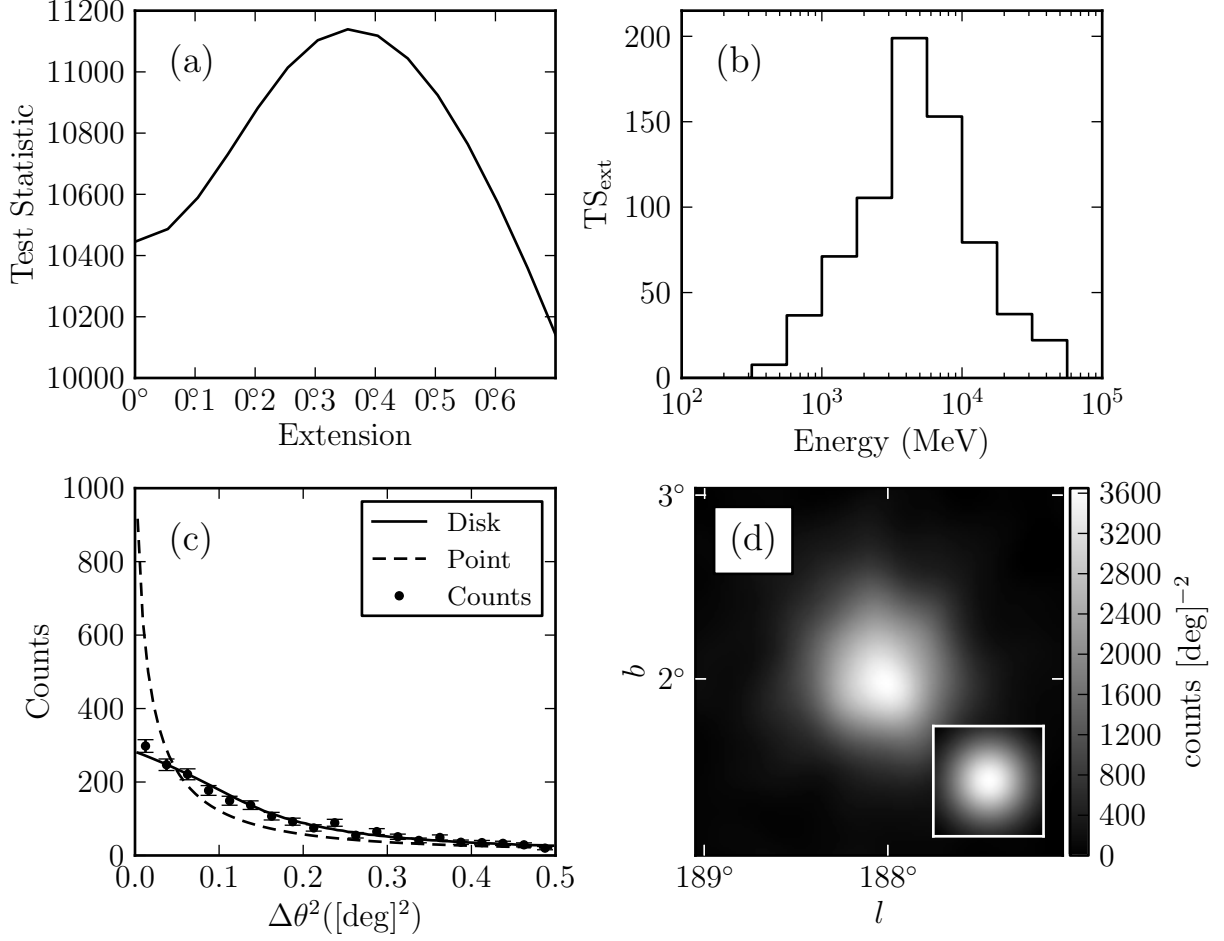


Fig. 1.— Counts maps and test statistic profiles for the SNR IC443. (a) TS vs. extension of the source. (b) TS<sub>ext</sub> for individual energy bands. (c) observed radial profile of counts in comparison to the expected profiles for a spatially extended source (solid and colored red in the online version) and for a point-like source (dashed and colored blue in the online version). (d) smoothed count map after subtraction of the diffuse emission compared to the smoothed LAT PSF (inset). Both were smoothed by a 0.1° 2D Gaussian kernel. Plots (a), (c), and (d) use only photons with energies between 1 GeV and 100 GeV. Plots (c) and (d) use only photons which converted in the front part of the tracker and have an improved angular resolution.



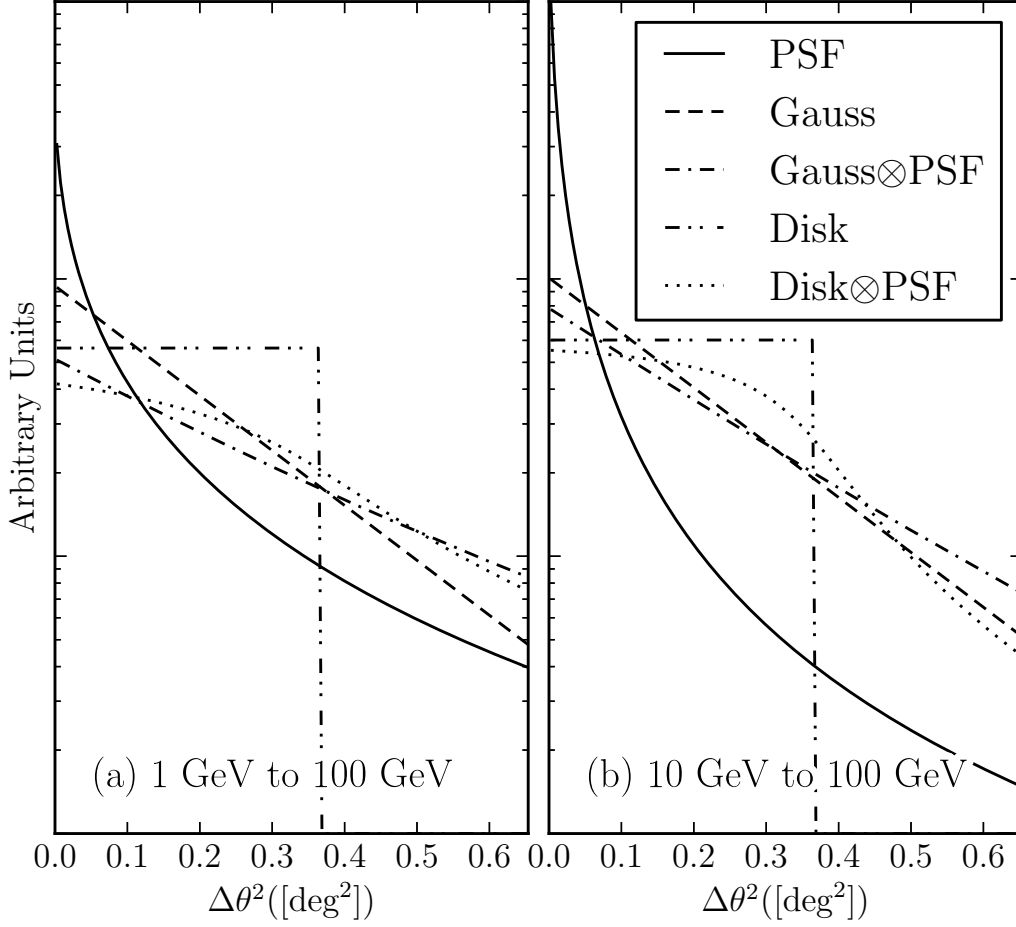


Fig. 2.— A comparison of a 2D Gaussian and uniform surface brightness profiles of extended sources before and after convolving with the PSF for two energy ranges. The solid black line is the PSF that would be observed for a power-law source of spectral index 2. The dashed line and the dash-dotted lines are the brightness profile of a Gaussian with  $r_{68} = 0.5$  and the convolution of this profile with the LAT PSF respectively (colored red in the online version). The dash-dot-dotted and the dot-dotted lines are the brightness profile of a uniform disk with  $r_{68} = 0.5$  and the convolution of this profile with the LAT PSF respectively (colored blue in the online version).

Table 1. Monte Carlo Spectral Parameters

| Spectral Index | Flux <sup>(a)</sup><br>(ph cm <sup>-2</sup> s <sup>-1</sup> ) | $N_{\text{sims}}$ | $\langle \text{TS} \rangle$ |
|----------------|---|-------------------|-----------------------------|
| 1.5            | $10^{-6}$   | 31952             | 92862                       |
|                | $3 \times 10^{-7}$  | 31962             | 22169                       |
|                | $10^{-7}$   | 31977             | 5806                        |
|                | $3 \times 10^{-8}$  | 31991             | 1270                        |
|                | $10^{-8}$   | 31940             | 301                         |
|                | $3 \times 10^{-9}$  | 30324             | 62                          |
| 2              | $10^{-6}$   | 31872             | 22067                       |
|                | $3 \times 10^{-7}$  | 31890             | 4898                        |
|                | $10^{-7}$   | 31858             | 1097                        |
|                | $3 \times 10^{-8}$  | 31632             | 236                         |
|                | $10^{-8}$   | 27491             | 103                         |
| 2.5            | $10^{-6}$   | 31822             | 4706                        |
|                | $3 \times 10^{-7}$  | 31822             | 889                         |
|                | $10^{-7}$   | 31169             | 176                         |
|                | $3 \times 10^{-8}$  | 21591             | 41                          |
| 3              | $10^{-6}$   | 31763             | 929                         |
|                | $3 \times 10^{-7}$  | 31665             | 161                         |
|                | $10^{-7}$   | 19271             | 40                          |

<sup>(a)</sup>Integral 1 GeV to 100 GeV flux.

Note. — A list of the spectral models of the simulated point-like sources which were tested for extension. For each model, the number of statistically independent simulations and the average value of TS is also tabulated. The models span representative spectral parameters.

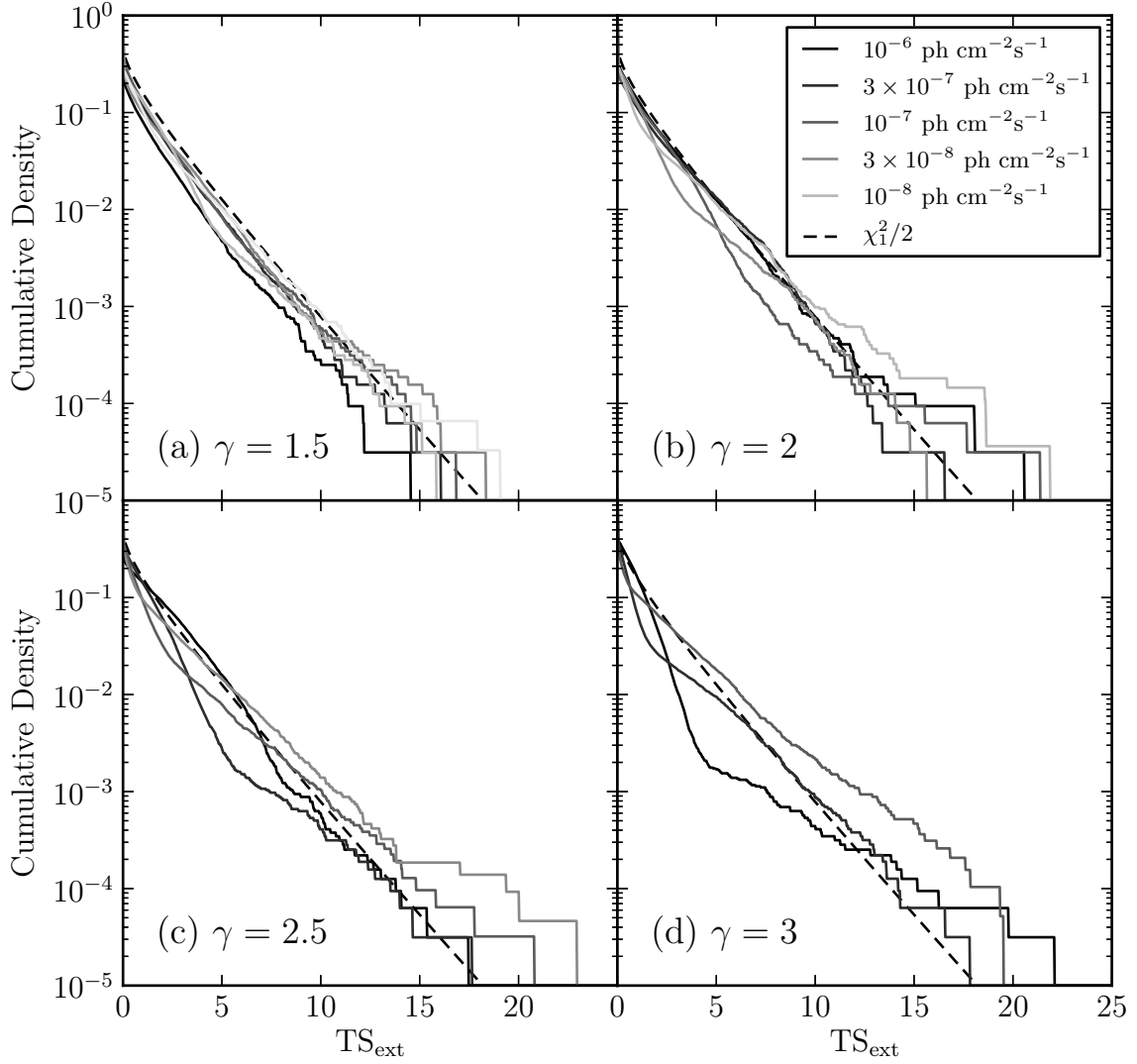


Fig. 3.— Distribution of the test statistic for the extension test. The four plots represent simulated point-like sources of different spectral indices and the different lines (colored in the online version) represent point-like sources with different 100 MeV to 100 GeV integral fluxes. The dashed line (colored red) is the cumulative density function of Equation 8.

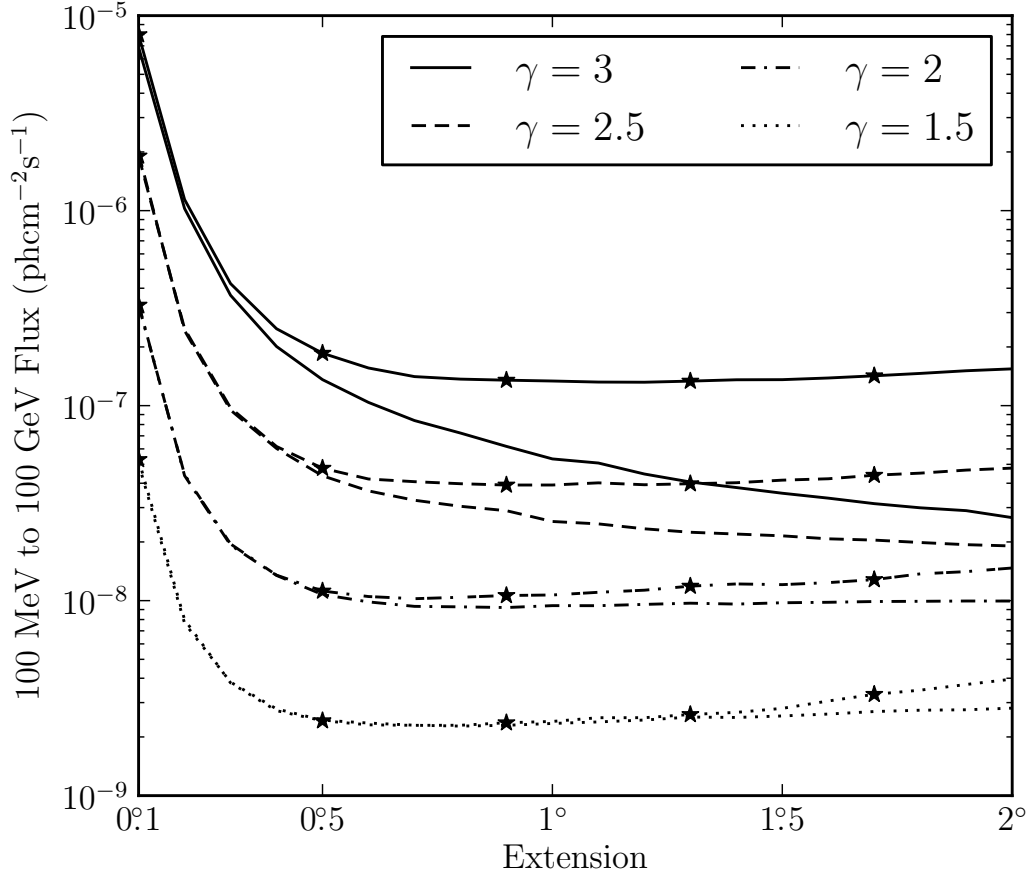


Fig. 4.— The detection threshold to resolve a uniform surface brightness profile extended source for a two-year exposure. All sources have an assumed power-law spectrum and the different line styles (colors in the electronic version) correspond to different simulated spectral indices. The lines with no markers correspond to the detection threshold using photons with energies between 100 MeV and 100 GeV while the lines with star-shaped markers correspond to the threshold using photons with energies between 1 GeV and 100 GeV.

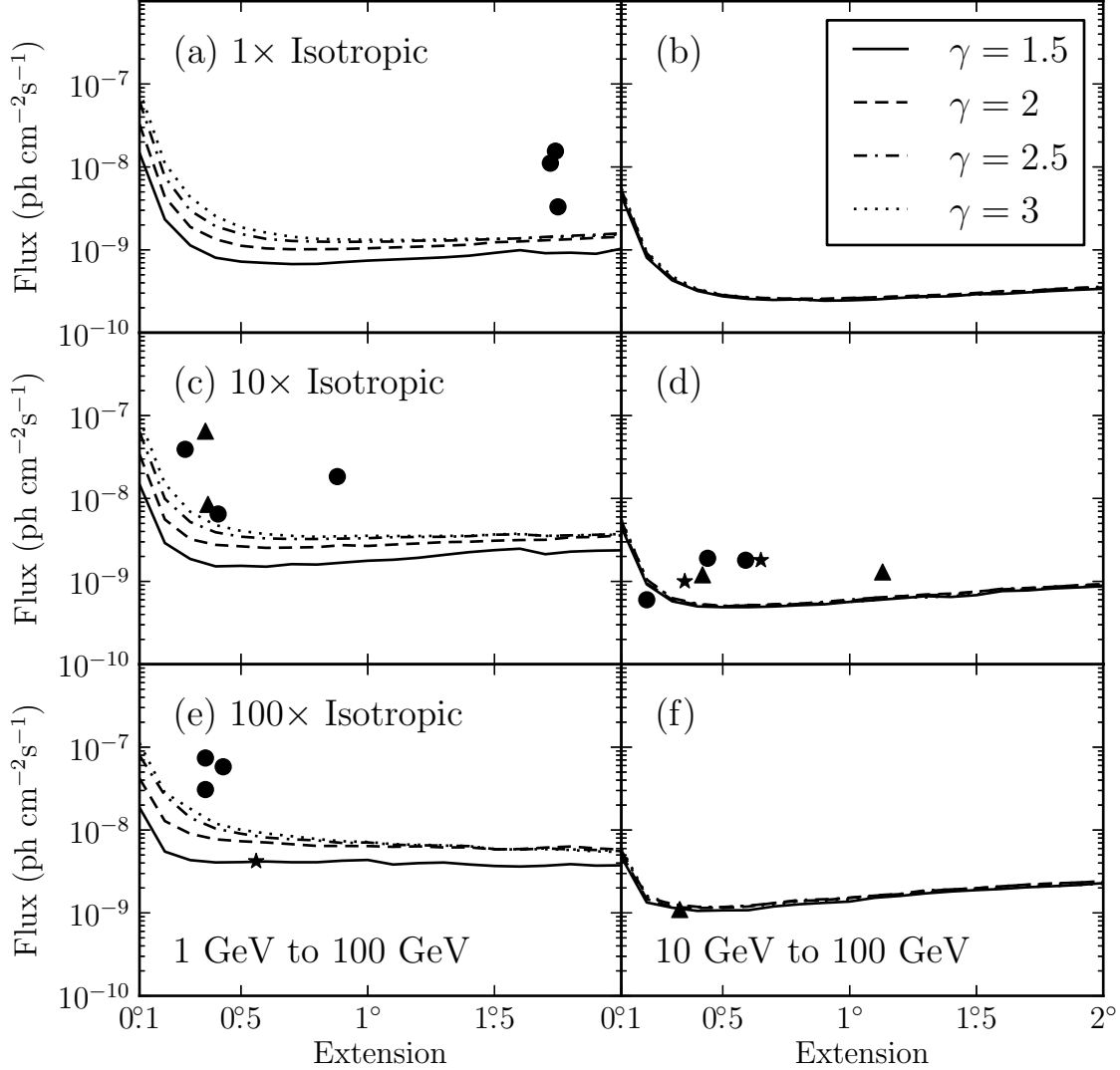


Fig. 5.— the LAT detection threshold for four spectral indices and three background ( $1\times$ ,  $10\times$ , and  $100\times$  the Sreekumar-like isotropic background) for a two-year exposure. The left plots are the detection threshold when using photons with energies between 1 GeV and 100 GeV and the right plots are the detection threshold when using photons with energies between 10 GeV and 100 GeV. The flux is integrated only in the selected energy range. Overlaid on this plot are the LAT detected extended sources placed by the magnitude of the nearby Galactic diffuse emission and the energy range they were analyzed with. The star-shaped markers (colored red in the electronic version) are sources with a spectral index closer to 1.5, the triangular markers (colored blue) an index closer to 2, and the circular markers (colored green) an index closer to 2.5. The circular marker in plot (d) below the sensitivity line is MSH 15–52.

Table 2. Extension Detection Threshold

| $\gamma$ | BG   | 0.1    | 0.2   | 0.3   | 0.4   | 0.5   | 0.6  | 0.7  | 0.8  | 0.9  | 1.0  | 1.1  | 1.2  | 1.3  | 1.4  | 1.5  | 1.6  | 1.7  | 1.8  | 1.9  | 2.0  |
|----------|------|--------|-------|-------|-------|-------|------|------|------|------|------|------|------|------|------|------|------|------|------|------|------|
| E>1 GeV  |      |        |       |       |       |       |      |      |      |      |      |      |      |      |      |      |      |      |      |      |      |
| 1.5      | 1×   | 148.1  | 23.3  | 11.3  | 8.0   | 7.2   | 6.9  | 6.7  | 6.8  | 7.1  | 7.4  | 7.6  | 7.9  | 8.1  | 8.5  | 9.2  | 9.9  | 9.1  | 9.2  | 9.0  | 10.3 |
|          | 10×  | 148.4  | 29.0  | 18.7  | 15.2  | 15.4  | 15.0 | 16.1 | 16.0 | 16.8 | 17.7 | 18.2 | 19.3 | 20.9 | 22.5 | 23.8 | 24.8 | 21.3 | 22.8 | 23.4 | 23.7 |
|          | 100× | 186.8  | 55.0  | 43.4  | 40.7  | 41.0  | 41.8 | 40.9 | 40.9 | 42.7 | 43.6 | 38.4 | 39.9 | 40.6 | 38.4 | 36.9 | 36.3 | 37.1 | 38.8 | 37.2 | 37.6 |
| 2        | 1×   | 328.4  | 43.4  | 18.9  | 13.4  | 11.2  | 10.4 | 10.2 | 10.2 | 10.2 | 10.4 | 10.7 | 10.9 | 11.2 | 11.5 | 12.4 | 12.6 | 13.0 | 13.4 | 14.0 | 14.4 |
|          | 10×  | 341.0  | 55.9  | 32.3  | 27.6  | 26.5  | 25.4 | 25.6 | 25.9 | 27.4 | 26.8 | 27.8 | 28.7 | 29.8 | 30.1 | 31.0 | 31.5 | 31.7 | 34.0 | 34.3 | 35.9 |
|          | 100× | 420.5  | 128.3 | 90.2  | 77.3  | 73.3  | 70.8 | 67.5 | 64.3 | 64.2 | 64.1 | 62.8 | 63.6 | 61.7 | 61.9 | 58.4 | 59.0 | 61.4 | 63.3 | 60.1 | 58.1 |
| 2.5      | 1×   | 627.1  | 75.6  | 29.8  | 19.3  | 15.5  | 13.5 | 12.8 | 12.6 | 12.5 | 12.5 | 12.6 | 12.9 | 12.9 | 13.1 | 13.5 | 13.7 | 14.3 | 14.8 | 15.2 | 15.8 |
|          | 10×  | 638.9  | 99.1  | 52.1  | 39.1  | 34.6  | 33.0 | 32.5 | 32.5 | 32.8 | 33.2 | 34.1 | 34.3 | 34.5 | 35.1 | 36.6 | 36.9 | 35.5 | 36.0 | 36.5 | 37.3 |
|          | 100× | 795.0  | 262.1 | 140.9 | 104.3 | 90.4  | 81.2 | 77.2 | 75.1 | 69.7 | 70.9 | 66.5 | 65.6 | 64.9 | 64.0 | 58.9 | 58.1 | 60.2 | 58.4 | 57.5 | 55.8 |
| 3        | 1×   | 841.5  | 110.6 | 43.2  | 25.5  | 18.7  | 16.1 | 14.4 | 13.6 | 13.3 | 13.2 | 13.1 | 13.1 | 13.4 | 13.6 | 13.5 | 13.8 | 14.2 | 14.4 | 14.8 | 15.4 |
|          | 10×  | 921.6  | 151.3 | 69.1  | 47.8  | 40.7  | 37.1 | 35.5 | 34.5 | 35.1 | 35.5 | 35.3 | 35.3 | 35.4 | 35.5 | 36.8 | 37.6 | 35.3 | 35.4 | 36.3 | 36.6 |
|          | 100× | 1124.1 | 282.9 | 181.1 | 119.8 | 100.7 | 91.1 | 84.3 | 77.9 | 73.3 | 71.8 | 67.6 | 66.4 | 65.5 | 63.9 | 59.0 | 58.6 | 58.8 | 57.5 | 55.4 | 54.4 |
| E>10 GeV |      |        |       |       |       |       |      |      |      |      |      |      |      |      |      |      |      |      |      |      |      |
| 1.5      | 1×   | 44.6   | 8.0   | 4.3   | 3.2   | 2.7   | 2.6  | 2.5  | 2.5  | 2.4  | 2.5  | 2.5  | 2.6  | 2.7  | 2.8  | 2.9  | 2.9  | 3.1  | 3.2  | 3.3  | 3.4  |
|          | 10×  | 45.2   | 9.2   | 5.8   | 5.0   | 4.9   | 4.9  | 5.0  | 5.2  | 5.3  | 5.7  | 5.9  | 6.3  | 6.6  | 6.5  | 6.8  | 7.6  | 7.8  | 8.2  | 8.5  | 8.7  |
|          | 100× | 47.3   | 13.4  | 11.6  | 10.6  | 10.8  | 10.8 | 12.0 | 12.7 | 13.2 | 13.7 | 15.3 | 16.1 | 17.2 | 18.2 | 18.9 | 19.5 | 20.4 | 21.0 | 21.7 | 22.9 |
| 2        | 1×   | 49.7   | 8.4   | 4.4   | 3.3   | 2.8   | 2.6  | 2.6  | 2.6  | 2.6  | 2.6  | 2.7  | 2.7  | 2.8  | 2.9  | 3.0  | 3.2  | 3.2  | 3.4  | 3.5  | 3.5  |
|          | 10×  | 48.6   | 9.5   | 6.0   | 5.2   | 5.0   | 5.2  | 5.2  | 5.3  | 5.4  | 5.8  | 6.4  | 6.6  | 7.0  | 7.1  | 7.5  | 8.0  | 8.3  | 8.6  | 9.0  | 9.2  |
|          | 100× | 51.8   | 14.7  | 11.8  | 11.5  | 11.5  | 11.9 | 13.2 | 14.0 | 14.3 | 15.3 | 16.2 | 16.9 | 18.4 | 19.2 | 19.8 | 21.0 | 22.0 | 22.8 | 23.2 | 24.3 |
| 2.5      | 1×   | 53.1   | 9.1   | 4.5   | 3.3   | 2.8   | 2.7  | 2.6  | 2.5  | 2.5  | 2.6  | 2.7  | 2.7  | 2.8  | 2.8  | 2.9  | 3.1  | 3.2  | 3.3  | 3.5  | 3.6  |
|          | 10×  | 53.7   | 10.5  | 6.3   | 5.4   | 5.1   | 5.1  | 5.3  | 5.4  | 5.7  | 6.0  | 6.3  | 6.6  | 6.8  | 6.9  | 7.5  | 8.1  | 8.3  | 8.6  | 8.9  | 9.2  |
|          | 100× | 57.0   | 15.6  | 12.7  | 11.9  | 11.8  | 12.2 | 13.1 | 14.3 | 14.6 | 15.2 | 16.3 | 17.0 | 18.8 | 19.2 | 19.9 | 21.0 | 21.9 | 22.3 | 23.3 | 23.7 |
| 3        | 1×   | 55.5   | 9.4   | 4.8   | 3.4   | 2.9   | 2.7  | 2.6  | 2.5  | 2.5  | 2.5  | 2.6  | 2.7  | 2.7  | 2.8  | 2.9  | 3.0  | 3.1  | 3.2  | 3.4  | 3.4  |
|          | 10×  | 56.0   | 10.5  | 6.2   | 5.3   | 5.1   | 5.1  | 5.1  | 5.3  | 5.5  | 5.7  | 5.9  | 6.4  | 6.4  | 6.6  | 7.0  | 7.8  | 8.0  | 8.3  | 8.6  | 8.9  |
|          | 100× | 60.3   | 16.2  | 12.7  | 11.7  | 11.8  | 12.2 | 12.6 | 13.8 | 14.2 | 14.6 | 15.8 | 16.5 | 17.6 | 18.5 | 19.4 | 19.8 | 20.7 | 21.0 | 21.8 | 22.5 |

Note. — The detection threshold to resolve spatially extended sources with a uniform surface brightness profile for a two-year exposure. The threshold is calculated for sources of varying energy ranges, spectral indices, and background levels. The sensitivity was calculated against a Sreekumar-like isotropic background and the second column is the factor that the simulated background was scaled by. The remaining columns are varying sizes of the source. The table quotes integral fluxes in the analyzed energy range (1 GeV to 100 GeV or 10 GeV to 100 GeV) in units of  $10^{-10} \text{ ph cm}^{-2} \text{ s}^{-1}$ .

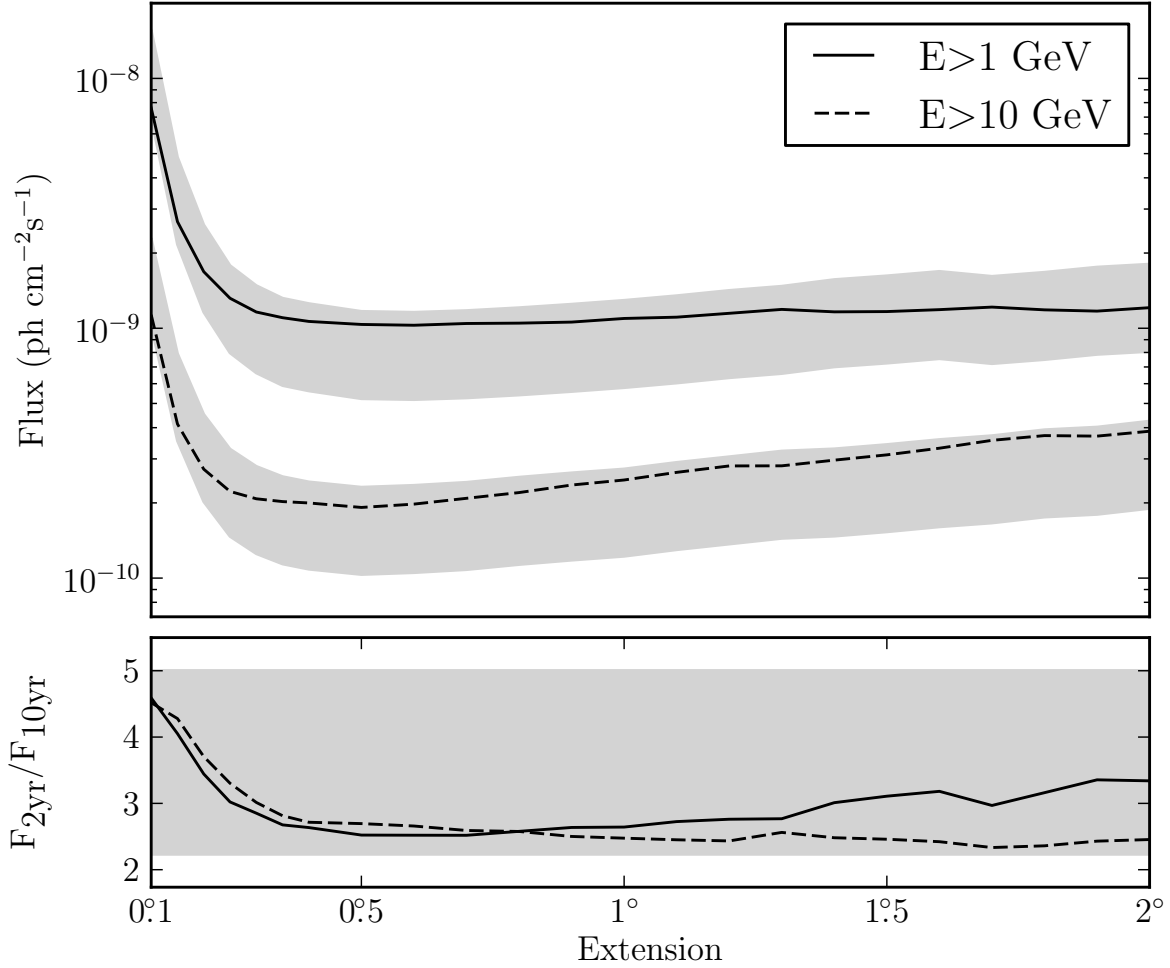


Fig. 6.— The projected detection threshold of the LAT to extension after a ten-year exposure for a power-law source of spectral index 2 against 10 times the isotropic background in the energy range from 1 GeV to 100 GeV (solid line colored red in the electronic version) and 10 GeV to 100 GeV (dashed line colored blue). The shaded gray regions represent the detection threshold assuming the sensitivity improves from 2 to 10 years by the square root of the exposure (top edge) and linearly with exposure (bottom edge). The lower plot shows the factor increase in sensitivity. For small extended sources, our detection threshold to the extension of a source will improve by a factor larger than the square root of the exposure.



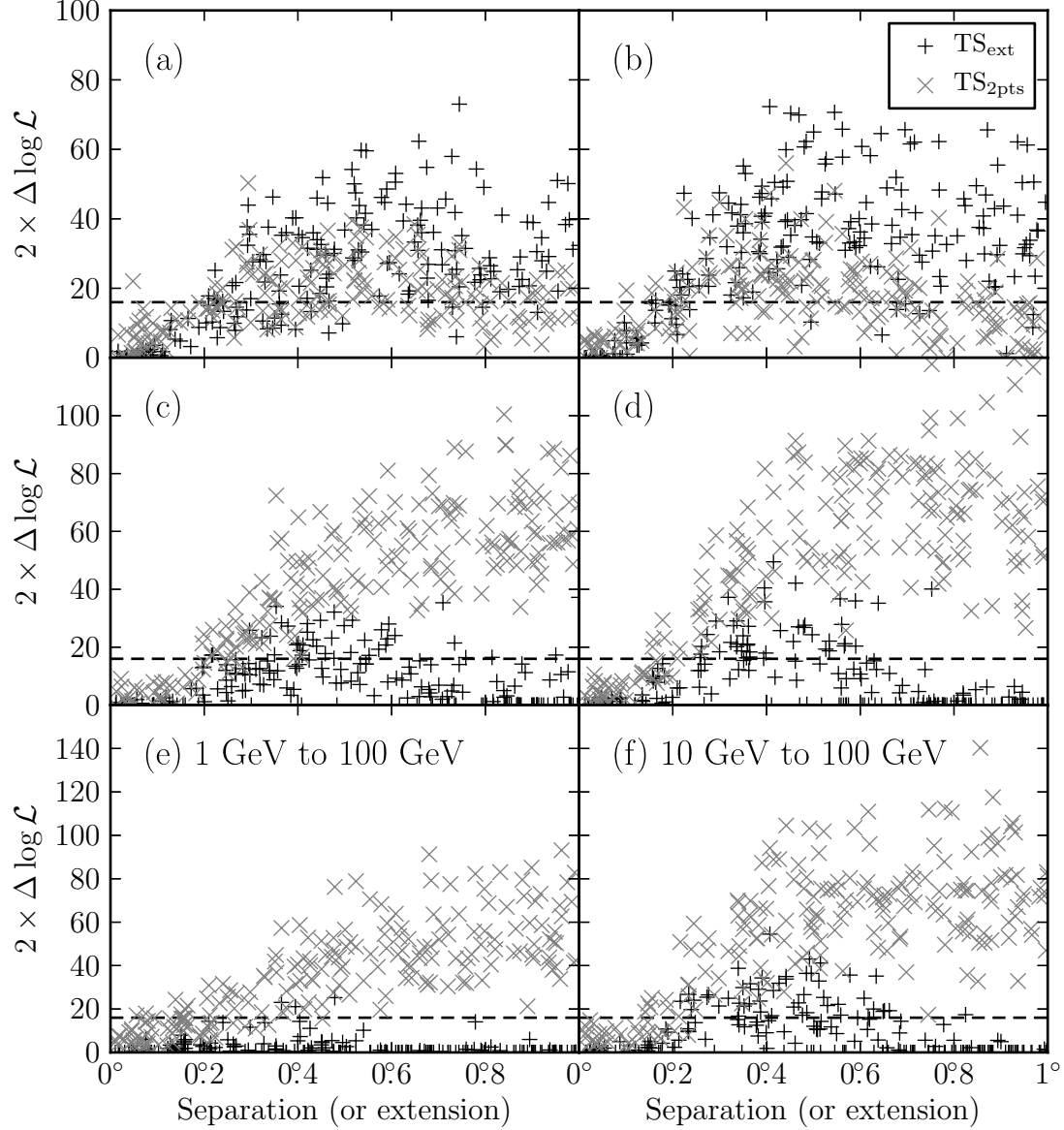


Fig. 7.— The distribution of  $TS_{\text{ext}}$  and  $TS_{2\text{pts}}$  (a) and (b) when fitting simulated spatially extended sources with radially-symmetric uniform intensity surface profiles and varying the source's size and (c), (d), (e), and (f) when fitting two simulated point-like sources and varying their separation distance. (c), and (d) represent simulations of two point-like sources with the same spectral index and (e), and (f) represent simulations of two point-like sources with different spectral indices. (a), (c), and (e) fit the simulated sources in the 1 GeV to 100 GeV energy range and (b), (d), and (f) when fitting the simulated sources in the 10 GeV to 100 GeV energy range.

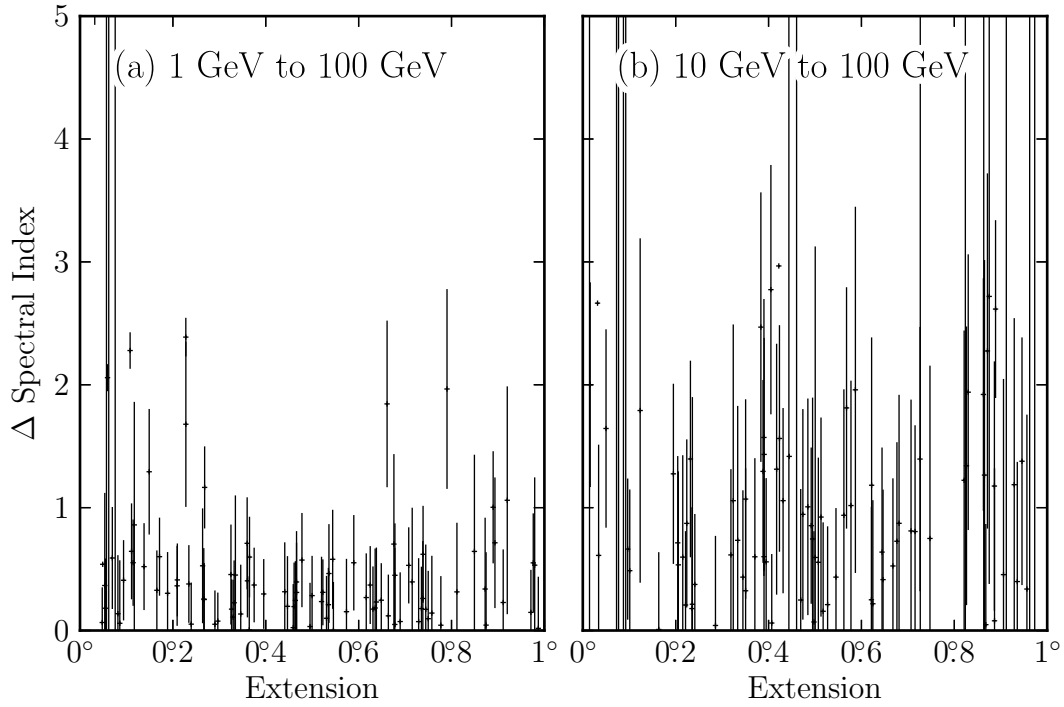


Fig. 8.— **The absolute value of the difference of the fit spectral index when fitting the simulated extended sources from figure 7 as two point-like sources for the first 100 simulated extended sources. The errors on the difference in spectral index were obtained by adding in quadrature the error on each spectral index. (a) represents the difference in index when analyzing the simulated extended sources in figure 7a in the 1 GeV to 100 GeV energy range whereas (b) represents the difference for the sources in figure 7a in the 10 GeV to 100 GeV energy range.**

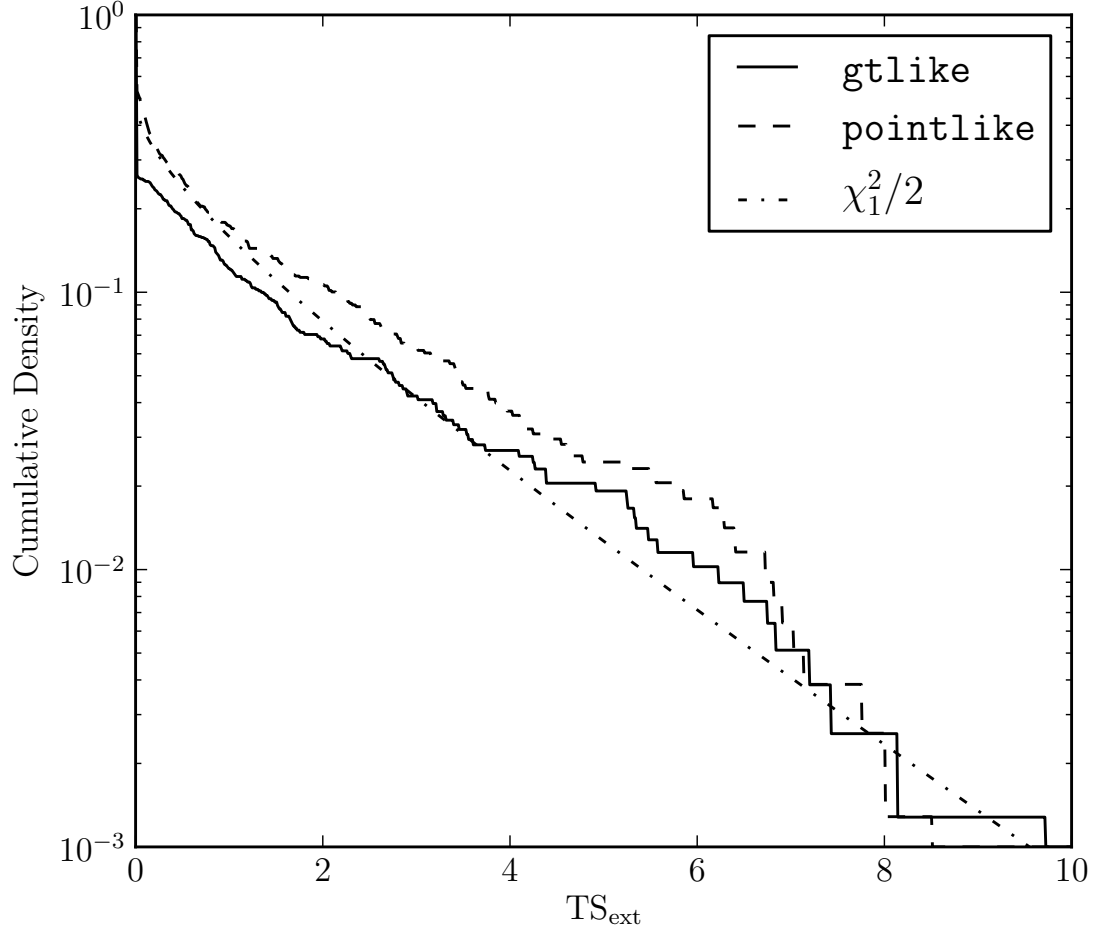


Fig. 9.— The cumulative density of  $TS_{\text{ext}}$  for the 783 clean AGN in 2LAC that were significant above 1 GeV calculated with `pointlike` (dashed line colored blue in the electronic version) and with `gtlike` (solid line colored red). AGN are too far and too small to be resolved by the LAT. Therefore, the cumulative density of  $TS_{\text{ext}}$  is expected to follow a  $\chi^2_1/2$  distribution (Equation 8, the dash-dotted line colored red).

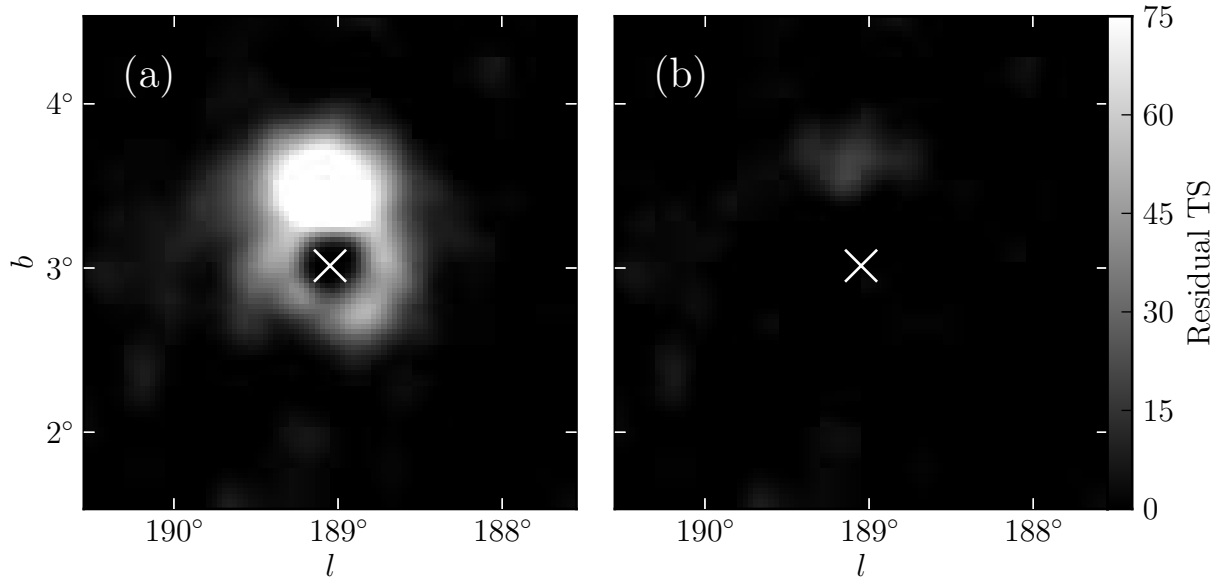


Fig. 10.— **A test statistic map generated for the region around the SNR IC443 using photons with energies between 1 GeV and 100 GeV. (a) test statistic map after subtracting IC443 modeled as a point-like source. (b) same as (a), but IC443 modeled as an extended source. The cross represents the best fit position of IC443.**

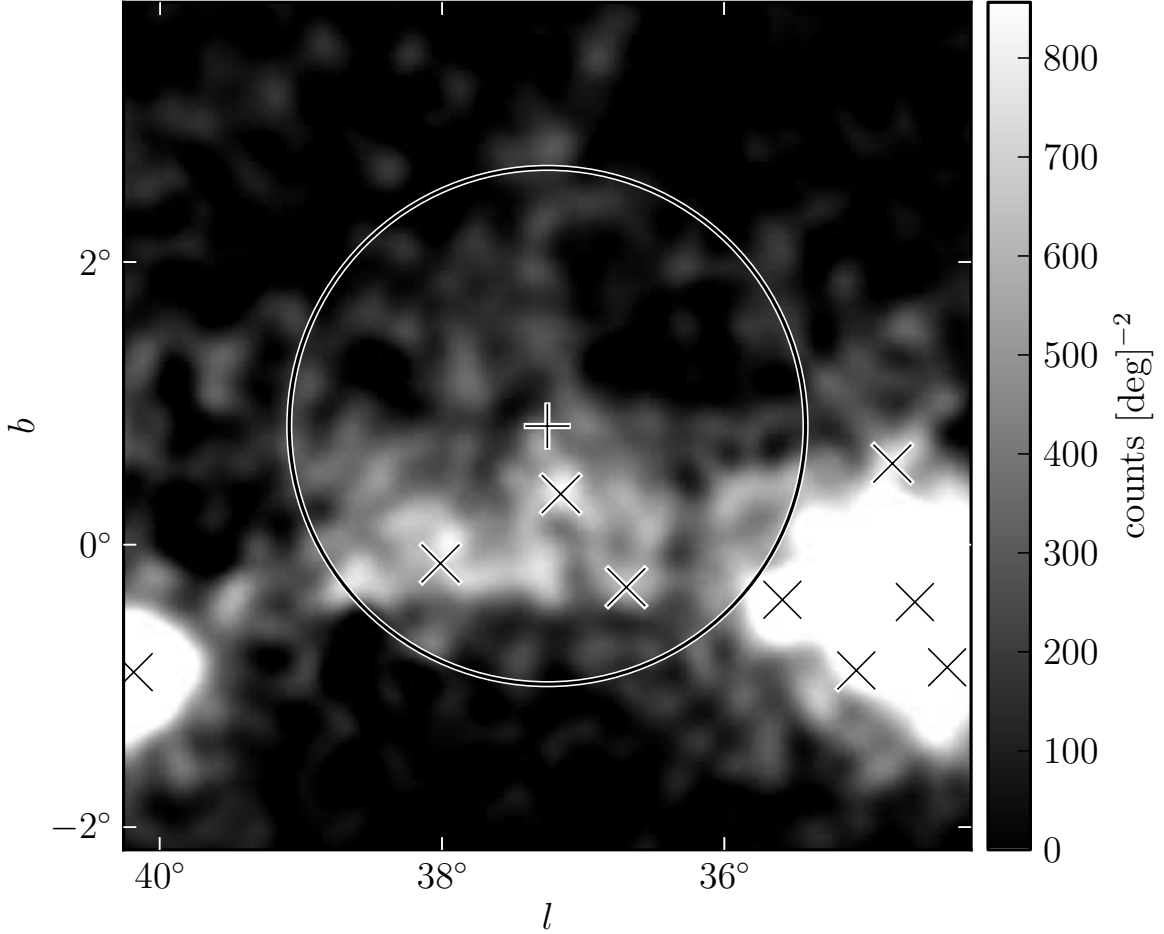


Fig. 11.— A diffuse-emission-subtracted 1 GeV to 100 GeV counts map of the region around 2FGL J1856.2+0450c smoothed by a  $0.1^\circ$  2D Gaussian kernel. The plus-shaped marker and circle (colored red in the online version) represent the center and size of the best fit radially-symmetric source with a uniform intensity profile. The black crosses represent the position of other 2FGL sources. The extension is statistically significant, but the extension encompasses many 2FGL sources and the emission does not look to be uniform. Although the fit is statistically significant, it likely corresponds to residual features of inaccurately modeled diffuse emission picked up by the fit.

Table 3. Analysis of the twelve extended sources included in 2FGL

| Name           | GLON<br>(deg.) | GLAT<br>(deg.) | $\sigma$<br>(deg.)       | TS      | TS <sub>ext</sub> | Pos Err<br>(deg.) | Flux <sup>(a)</sup> | Index           |
|----------------|----------------|----------------|--------------------------|---------|-------------------|-------------------|---------------------|-----------------|
| E>1 GeV        |                |                |                          |         |                   |                   |                     |                 |
| SMC            | 302.68         | -44.81         | $1.75 \pm 0.07 \pm 0.02$ | 94.8    | 67.4              | 0.12              | $3.3 \pm 0.4$       | $2.41 \pm 0.17$ |
| LMC            | 279.10         | -32.61         | $1.74 \pm 0.05 \pm 0.13$ | 1101.3  | 860.5             | 0.05              | $15.5 \pm 0.6$      | $2.48 \pm 0.06$ |
| IC443          | 189.05         | 3.04           | $0.36 \pm 0.01 \pm 0.04$ | 10719.8 | 510.4             | 0.01              | $64.8 \pm 1.2$      | $2.23 \pm 0.02$ |
| Vela X         | 263.34         | -3.11          | 0.88                     |         |                   |                   |                     |                 |
| Centarus A     | 309.52         | 19.42          | $\sim 10$                |         |                   |                   |                     |                 |
| W28            | 6.50           | -0.27          | $0.43 \pm 0.02 \pm 0.03$ | 1324.8  | 177.4             | 0.01              | $58.0 \pm 1.8$      | $2.63 \pm 0.03$ |
| W30            | 8.61           | -0.20          | $0.36 \pm 0.02 \pm 0.02$ | 465.4   | 73.3              | 0.02              | $30.7 \pm 1.6$      | $2.59 \pm 0.04$ |
| W44            | 34.69          | -0.38          | $0.36 \pm 0.01 \pm 0.02$ | 1903.3  | 217.7             | 0.01              | $73.6 \pm 1.8$      | $2.68 \pm 0.02$ |
| W51C           | 49.13          | -0.45          | $0.28 \pm 0.02 \pm 0.05$ | 1819.5  | 115.7             | 0.01              | $39.3 \pm 1.3$      | $2.35 \pm 0.03$ |
| Cygnus Loop    | 74.22          | -8.46          | $1.72 \pm 0.05 \pm 0.07$ | 356.5   | 356.5             | 0.06              | $11.1 \pm 0.7$      | $2.53 \pm 0.11$ |
| E>10 GeV       |                |                |                          |         |                   |                   |                     |                 |
| MSH15-52       | 320.38         | -1.22          | $0.20 \pm 0.04 \pm 0.03$ | 76.2    | 6.5               | 0.03              | $0.6 \pm 0.7$       | $2.27 \pm 0.73$ |
| HESS J1825-137 | 17.56          | -0.46          | $0.65 \pm 0.03 \pm 0.01$ | 83.6    | 55.9              | 0.05              | $1.8 \pm 0.2$       | $1.74 \pm 0.19$ |

<sup>(a)</sup>Integral Flux in units of  $10^{-9} \text{ph cm}^{-2} \text{s}^{-1}$  and integrated in the fit energy range (either 1 GeV 100 GeV or 10 GeV 100 GeV).

Note. — All sources were fit using a spatial model assuming a uniform radially symmetric intensity distribution. GLON and GLAT are Galactic longitude and latitude of the best fit extended source respectively. The first error on  $\sigma$  is statistical and the second is systematic (see Section 8). Pos Err is the error on the position of the source. Vela X and the Centarus A Lobes were not fit in our analysis but are include for completeness.

Table 4. Extension fit for the nine additional extended sources

| Name               | GLON<br>(deg.) | GLAT<br>(deg.) | $\sigma$<br>(deg.)       | TS    | TS <sub>ext</sub> | Pos Err<br>(deg.) | Flux <sup>(a)</sup> | Index           | Counterpart     |
|--------------------|----------------|----------------|--------------------------|-------|-------------------|-------------------|---------------------|-----------------|-----------------|
| E>1 GeV            |                |                |                          |       |                   |                   |                     |                 |                 |
| 2FGL J0823.0–4246  | 260.32         | -3.28          | $0.37 \pm 0.03 \pm 0.02$ | 320.9 | 46.3              | 0.02              | $8.5 \pm 0.7$       | $2.20 \pm 0.09$ | Puppis A        |
| 2FGL J1627.0–2425c | 353.08         | 16.78          | $0.41 \pm 0.05 \pm 0.02$ | 144.5 | 31.1              | 0.04              | $6.5 \pm 0.6$       | $2.49 \pm 0.14$ | Ophiuchus       |
| 2FGL J1712.4–3941  | 347.25         | -0.54          | $0.56 \pm 0.04 \pm 0.01$ | 75.0  | 39.6              | 0.05              | $4.2 \pm 0.9$       | $1.47 \pm 0.12$ | RX J1713.7–3946 |
| E>10 GeV           |                |                |                          |       |                   |                   |                     |                 |                 |
| 2FGL J0851.7–4635  | 266.29         | -1.43          | $1.13 \pm 0.08 \pm 0.05$ | 116.1 | 87.2              | 0.07              | $1.3 \pm 0.2$       | $1.76 \pm 0.21$ | Vela Jr.        |
| 2FGL J1615.0–5051  | 332.38         | -0.14          | $0.33 \pm 0.04 \pm 0.01$ | 53.4  | 16.3              | 0.04              | $1.1 \pm 0.2$       | $2.24 \pm 0.28$ | HESS J1616–508  |
| 2FGL J1615.2–5138  | 331.66         | -0.66          | $0.42 \pm 0.03 \pm 0.01$ | 76.6  | 48.0              | 0.05              | $1.2 \pm 0.2$       | $1.77 \pm 0.24$ | HESS J1614–518  |
| 2FGL J1632.4–4753c | 336.41         | 0.22           | $0.44 \pm 0.04 \pm 0.03$ | 127.8 | 64.5              | 0.04              | $1.9 \pm 0.2$       | $2.29 \pm 0.21$ | HESS J1632–478  |
| 2FGL J1837.3–0700c | 25.08          | 0.13           | $0.35 \pm 0.08 \pm 0.03$ | 46.2  | 18.8              | 0.07              | $1.0 \pm 0.2$       | $1.63 \pm 0.29$ | HESS J1837–069  |
| 2FGL J2021.5+4026  | 78.18          | 2.19           | $0.59 \pm 0.03 \pm 0.02$ | 222.2 | 116.4             | 0.04              | $1.8 \pm 0.2$       | $2.31 \pm 0.19$ | $\gamma$ -Cygni |

<sup>(a)</sup>Integral Flux in units of  $10^{-9}\text{ph cm}^{-2}\text{s}^{-1}$  and integrated in the fit energy range (either 1 GeV 100 GeV or 10 GeV 100 GeV).

Note. — The columns in this table have the same meaning as those in Table 3. **RX J1713.7–3946 and Vela Jr. were previously studied in dedicated publications (Abdo et al. 2011e,b).**

Table 5. Dual localization, alternative PSF, and alternative diffuse results

| Name               | TS <sub>pointlike</sub> | TS <sub>gtlike</sub> | TS <sub>alt,diff</sub> | TS <sub>extpointlike</sub> | TS <sub>extgtlike</sub> | TS <sub>extalt,diff</sub> | $\sigma$<br>(deg.) | $\sigma_{\text{alt,diff}}$<br>(deg.) | $\sigma_{\text{alt,psf}}$<br>(deg.) | TS <sub>2pts</sub> |
|--------------------|-------------------------|----------------------|------------------------|----------------------------|-------------------------|---------------------------|--------------------|--------------------------------------|-------------------------------------|--------------------|
| E>1 GeV            |                         |                      |                        |                            |                         |                           |                    |                                      |                                     |                    |
| 2FGL J0823.0–4246  | 350.9                   | 320.9                | 352.5                  | 66.0                       | 46.3                    | 53.6                      | 0.37               | 0.39                                 | 0.38                                | 22.1               |
| 2FGL J1627.0–2425c | 170.2                   | 144.5                | 112.6                  | 43.9                       | 31.1                    | 23.9                      | 0.41               | 0.40                                 | 0.39                                | 20.0               |
| 2FGL J1712.4–3941  | 80.9                    | 75.0                 | 43.4                   | 47.4                       | 39.6                    | 22.2                      | 0.56               | 0.56                                 | 0.54                                | 6.4                |
| E>10 GeV           |                         |                      |                        |                            |                         |                           |                    |                                      |                                     |                    |
| 2FGL J0851.7–4635  | 116.7                   | 116.1                | 122.3                  | 87.1                       | 87.2                    | 90.4                      | 1.13               | 1.16                                 | 1.17                                | 16.1               |
| 2FGL J1615.0–5051  | 52.4                    | 53.4                 | 55.6                   | 17.5                       | 16.3                    | 17.4                      | 0.33               | 0.32                                 | 0.32                                | 11.9               |
| 2FGL J1615.2–5138  | 76.3                    | 76.6                 | 86.3                   | 44.0                       | 48.0                    | 52.6                      | 0.42               | 0.43                                 | 0.43                                | 37.0               |
| 2FGL J1632.4–4753c | 126.6                   | 127.8                | 120.7                  | 63.9                       | 64.5                    | 64.1                      | 0.44               | 0.44                                 | 0.47                                | 40.6               |
| 2FGL J1837.3–0700c | 45.4                    | 46.2                 | 39.0                   | 18.5                       | 18.8                    | 16.6                      | 0.35               | 0.34                                 | 0.38                                | 12.6               |
| 2FGL J2021.5+4026  | 234.3                   | 222.2                | 235.6                  | 135.9                      | 116.4                   | 121.4                     | 0.59               | 0.60                                 | 0.60                                | 24.3               |

Note. — TS<sub>pointlike</sub>, TS<sub>gtlike</sub>, and TS<sub>alt,diff</sub> are the test statistic values from `pointlike`, `gtlike`, and `gtlike` with the alternate diffuse model respectively. TS<sub>extpointlike</sub>, TS<sub>extgtlike</sub>, and TS<sub>extalt,diff</sub> are the test statistic values of the extension test from `pointlike`, `gtlike`, and `gtlike` with the alternate diffuse model respectively.  $\sigma$ ,  $\sigma_{\text{alt,diff}}$ , and  $\sigma_{\text{alt,psf}}$  are the fit extension with the standard analysis, the alternate diffuse model, and the alternate PSF respectively. TS<sub>2pts</sub> is the test statistic for the two point-like source hypothesis test (see Section 5).



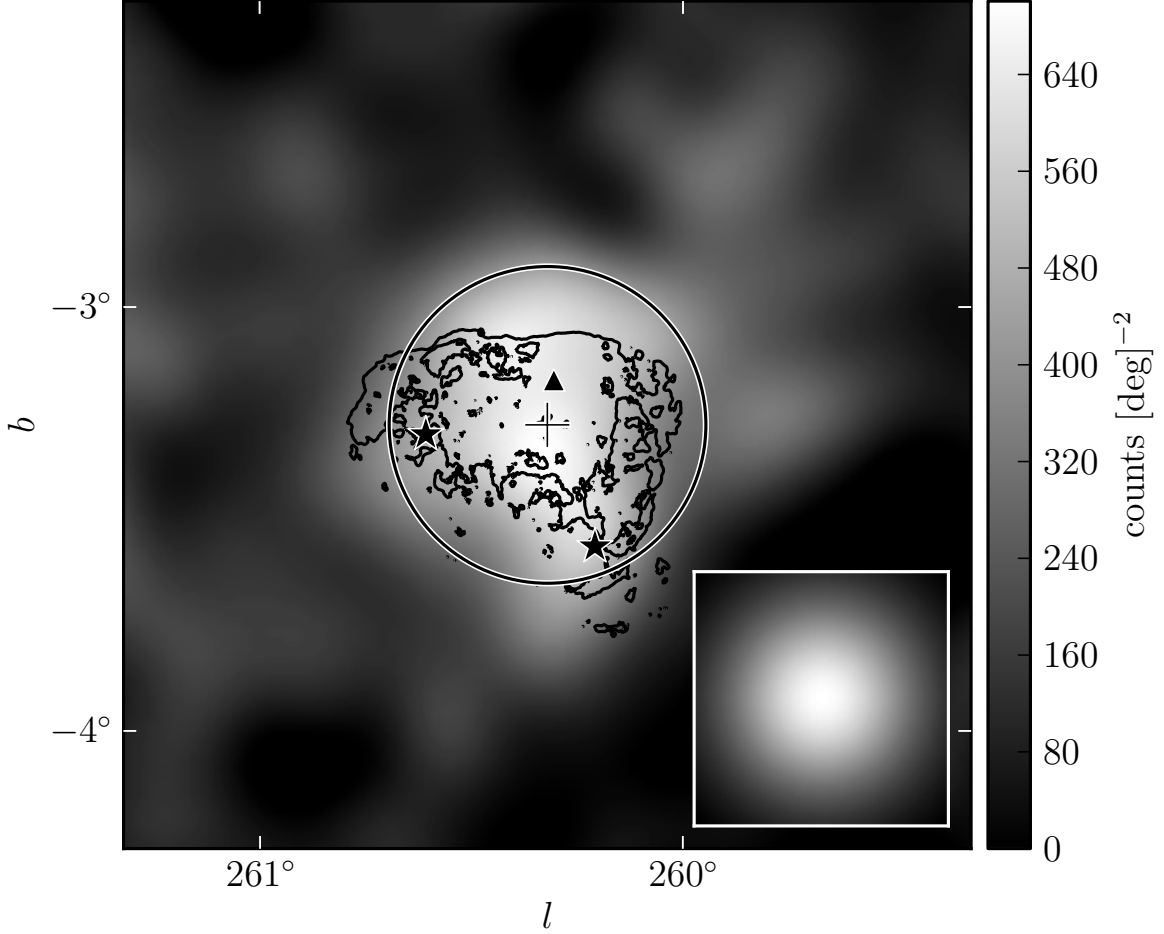


Fig. 12.— A diffuse-emission-subtracted 1 GeV to 100 GeV counts map of 2FGL J0823.0–4246 smoothed by a  $0.1^\circ$  2D Gaussian kernel. The triangular marker (colored red in the online version) represents the 2FGL position of this source. The plus-shaped marker and the circle (colored red) represent the best fit position and extension of this source assuming a radially-symmetric uniform surface brightness profile. The two star-shaped markers (colored green) represent 2FGL sources that were removed from the background model. The lower right inset is the model predicted emission from a point-like source with the same spectrum as 2FGL J0823.4–4305 smoothed by the same kernel. This source is spatially coincident with the Puppis A SNR. The light blue contours correspond to the X-ray image of Puppis A observed by *ROSAT* (Petre et al. 1996).

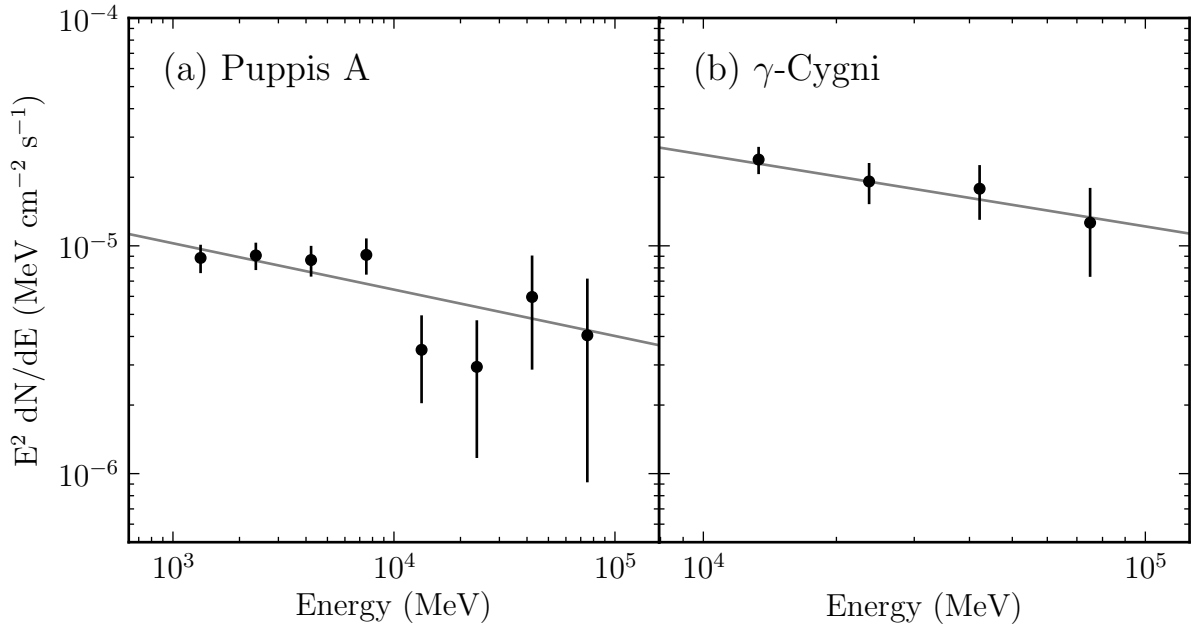


Fig. 13.— The spectral energy distribution of the extended sources Puppis A (2FGL J0823.0–4246) and  $\gamma$ -Cygni (2FGL J2021.5+4026). The lines (colored red in the online version) are the best fit power-law spectral models of these sources. The spectral errors are statistical only.

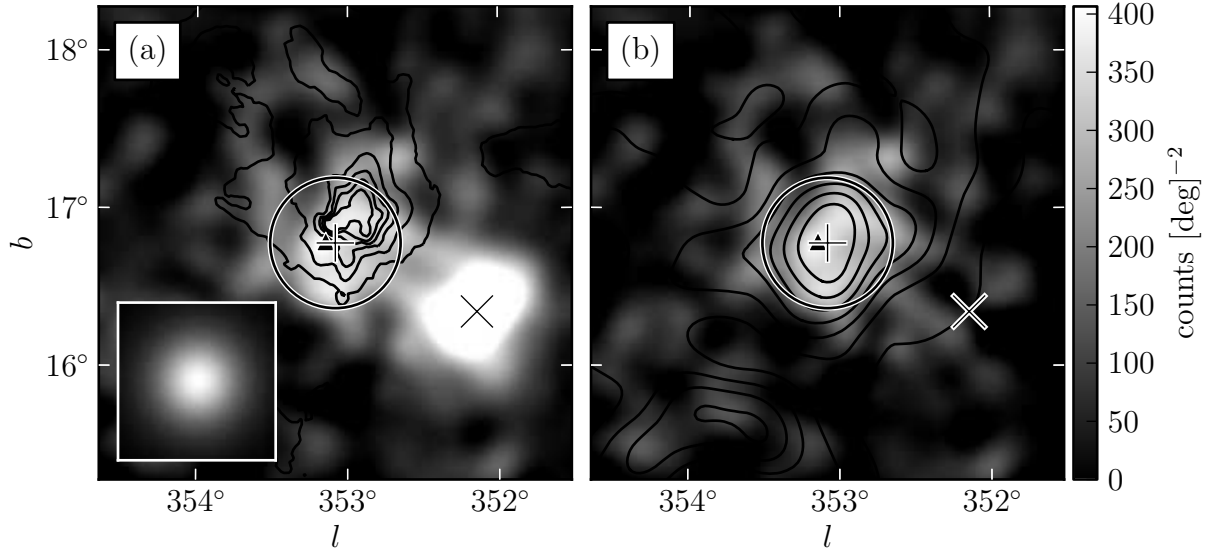


Fig. 14.— A diffuse-emission-subtracted 1 GeV to 100 GeV counts map of (a) the region around 2FGL J1627.0–2425 smoothed by a  $0.1^\circ$  2D Gaussian kernel (b) also the emission from 2FGL J1625.7–2526 subtracted. The triangular marker (colored red in the online version) represents the 2FGL position of this source. The plus-shaped marker and the circle (colored red) represent the best fit position and extension of this source assuming a radially-symmetric uniform surface brightness profile. The contours in (a) correspond to the 100 micrometer image observed by IRAS (Young et al. 1986). The contours in (b) correspond to  $^{12}\text{CO}$  ( $J = 1 \rightarrow 0$ ) emission integrated from  $-8$  km/s to  $20$  km/s. They are from de Geus et al. (1990), were cleaned using the moment-masking technique (Dame 2011), and have been smoothed by a  $0.25^\circ$  2D Gaussian kernel.

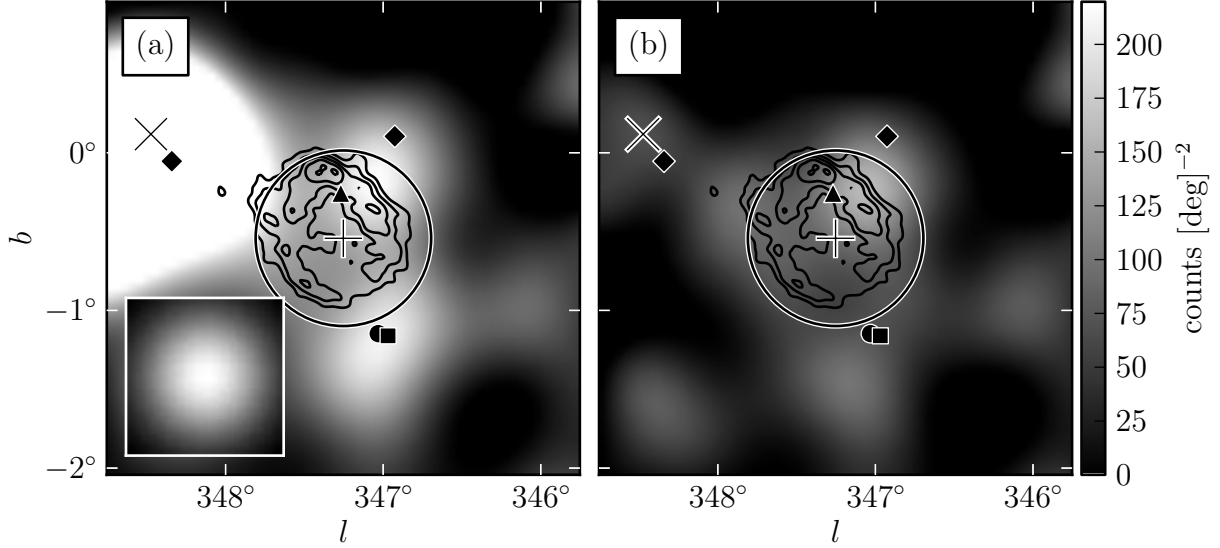


Fig. 15.— A diffuse-emission-subtracted 1 GeV to 100 GeV counts map of 2FGL J1712.4–3941 (a) smoothed by a 0.25 2D Gaussian kernel and (b) with the emission from the background sources subtracted. This source is spatially coincident with RX J1713.7–3946 and was recently studied in Abdo et al. (2011e). The triangular marker (colored red in the online version) represents the 2FGL position of this source. The plus-shaped marker and the circle (colored red) are the best fit position and extension of this source assuming a radially symmetric uniform surface brightness profile. The contours (colored light blue) correspond to the TeV image (Aharonian et al. 2007b). The region was analyzed with the same background model as Abdo et al. (2011e). Source A is coincident with 2FGL J1715.4–4024c and the circular and square-shaped marker (colored blue) represent the 2FGL and relocalized position of this source respectively. The diamond-shaped markers (colored purple) represent the position of source B and C that were added to the background model.

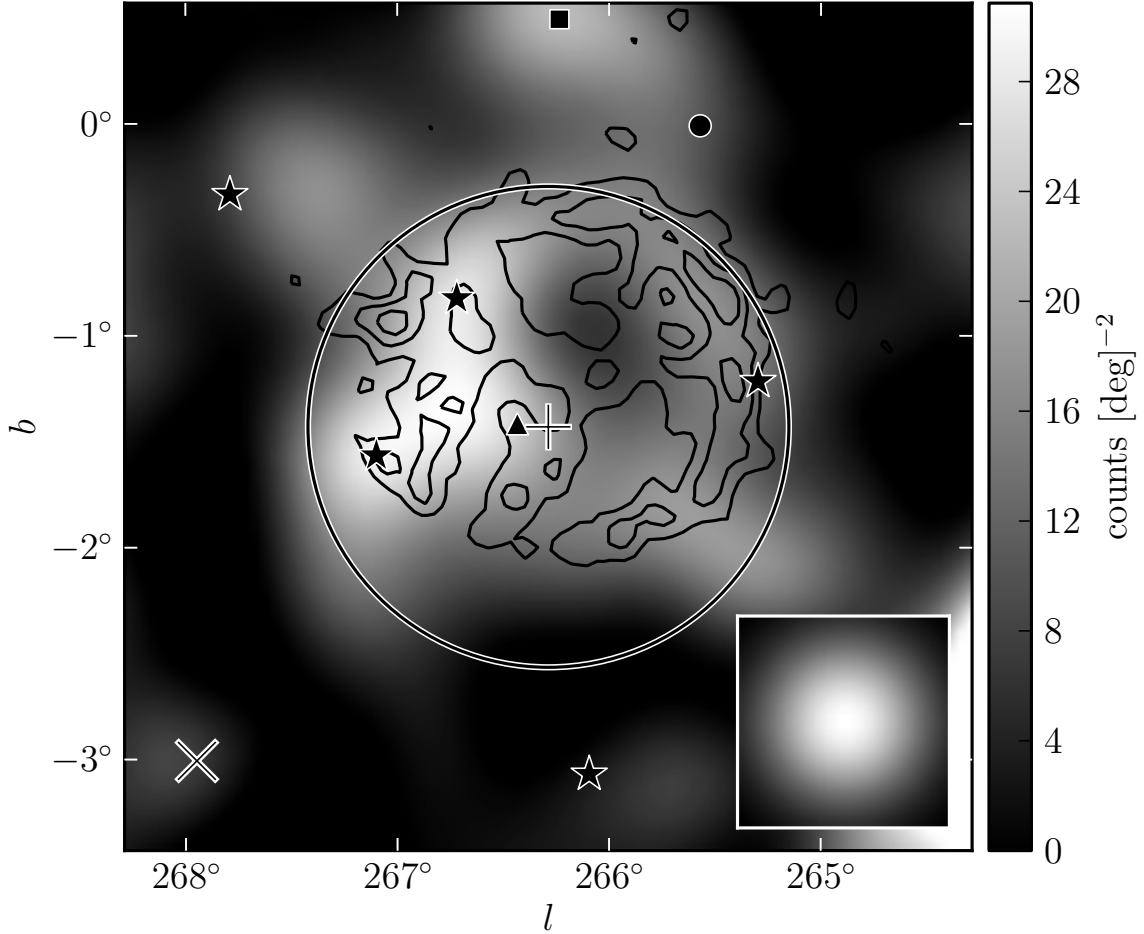


Fig. 16.— A diffuse-emission-subtracted 10 GeV to 100 GeV counts map of 2FGL J0851.7–4635 smoothed by a  $0.25^\circ$  2D Gaussian kernel. The triangular marker (colored red in the electronic version) represents the 2FGL position of this source. The plus-shaped marker and the circle (colored red) are the best fit position and extension of this source assuming a radially-symmetric uniform surface brightness profile. The five star-shaped markers (colored green) represent 2FGL sources that were removed from the background model. The circular and square marker (colored blue) represents the 2FGL and relocalized position of 2FGL J0854.7–4501 respectively. This extended source is spatially coincident with the Vela Jr. SNR. The contours (colored light blue) correspond to the TeV image of Vela Jr. (Aharonian et al. 2007a).

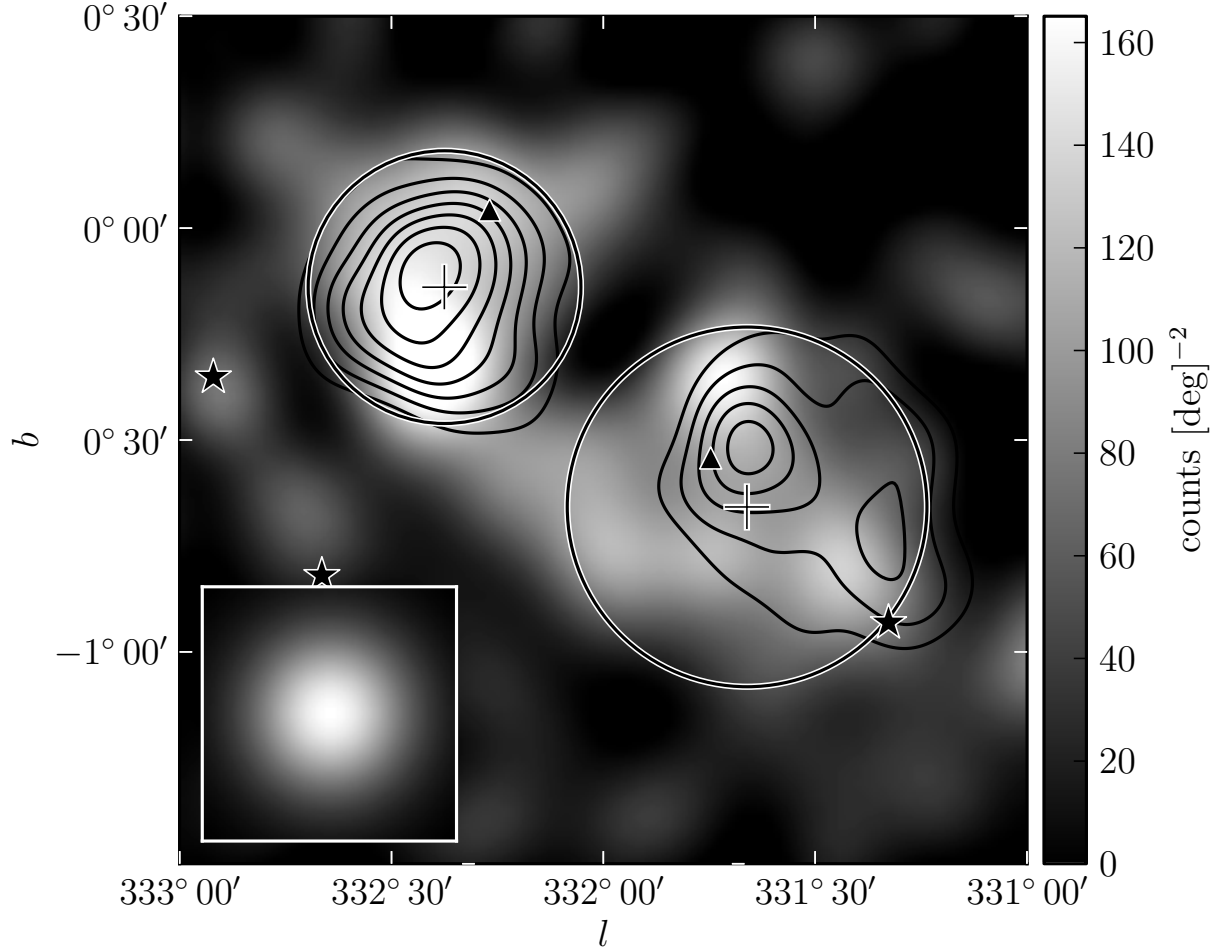


Fig. 17.— A diffuse-emission-subtracted 10 GeV to 100 GeV counts map of 2FGL J1615.0–5051 (upper left) and 2FGL J1615.2–5138 (lower right) smoothed by a  $0^\circ.1$  2D Gaussian kernel. The triangular markers (colored red in the electronic version) represent the 2FGL positions of these sources. The cross-shaped markers and the circles (colored red) represent the best fit positions and extensions of these sources assuming a radially symmetric uniform surface brightness profile. The three star-shaped markers (colored green) represent 2FGL sources that were removed from the background model. The contours (colored light blue) correspond to the TeV image of HESS J1616–508 (left) and HESS J1614–518 (right) (Aharonian et al. 2006).

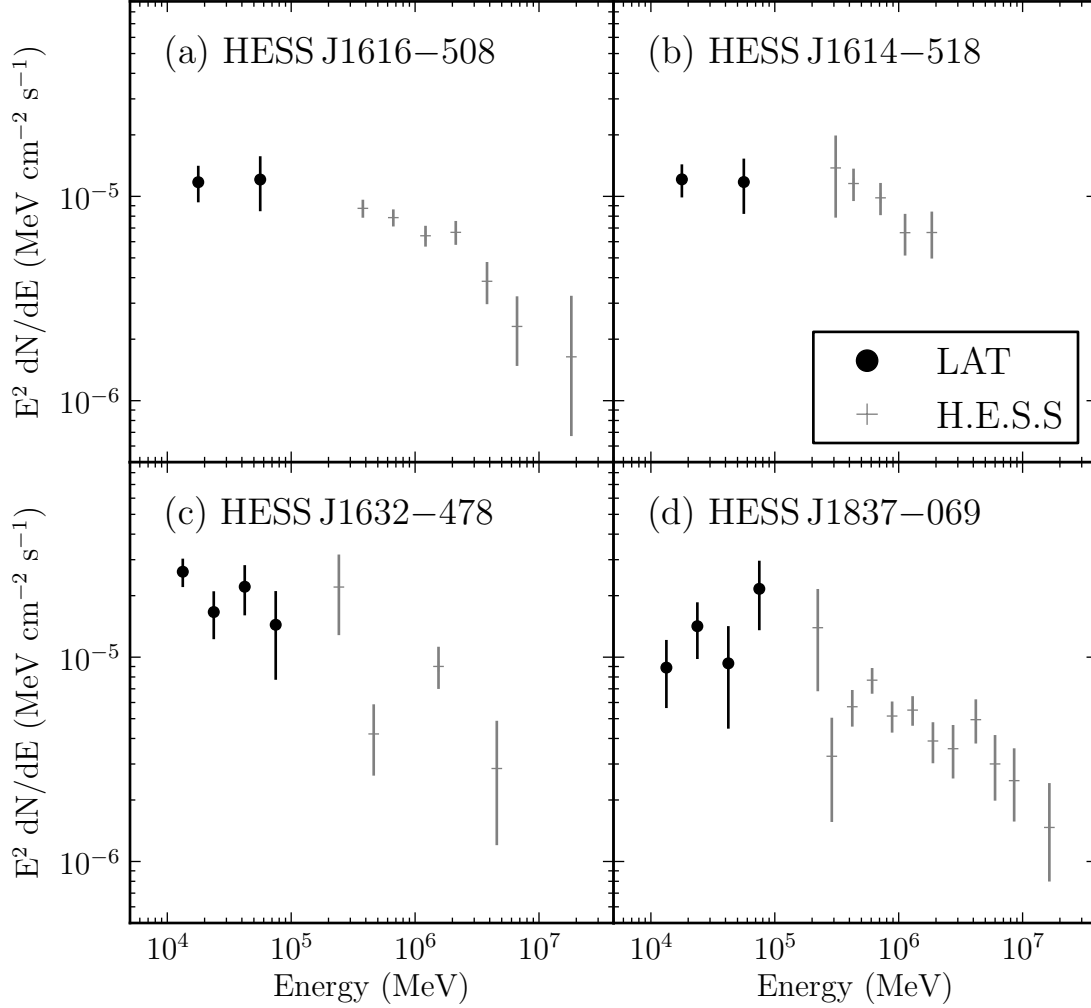


Fig. 18.— The spectral energy distribution of four extended sources associated with unidentified extended TeV sources. The black points with circular markers are obtained by the LAT. The points with plus-shaped markers (colored red in the electronic version) are for the associated H.E.S.S. sources. (a) the LAT SED of 2FGL J1615.0–5051 together with the H.E.S.S. SED of HESS J1616–508. (b) 2FGL J1615.2–5138 and HESS J1614–518. (c) 2FGL J1632.4–4753c and HESS J1632–478. (d) 2FGL J1837.3–0700c and HESS J1837–069. The H.E.S.S. data points are from (Aharonian et al. 2006). Both LAT and H.E.S.S. spectral errors are statistical only.

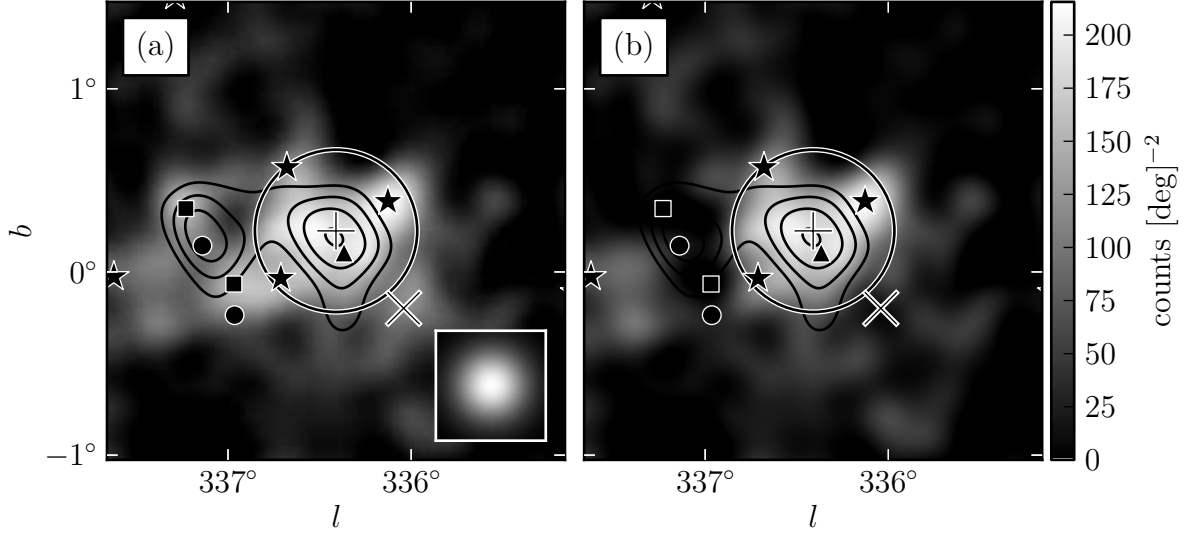


Fig. 19.— **A diffuse-emission-subtracted 10 GeV to 100 GeV counts map of 2FGL J1632.4–4753c (a) smoothed by a  $0.1^\circ$  2D Gaussian kernel and (b) with the emission from the background sources subtracted.** The triangular marker (colored red in the electronic version) represents the 2FGL position of this source. The plus-shaped marker and the circle (colored red) are the best fit position and extension of 2FGL J1632.4–4753c assuming a radially-symmetric uniform surface brightness profile. The four star-shaped markers (colored green) represent 2FGL sources that were removed from the background model. The circular and square markers (colored blue) represent the 2FGL and relocalized positions respectively of 2FGL J1635.4–4717c (left) and 2FGL J1636.3–4740c (right). The contours (colored light blue) correspond to the TeV image of HESS J1632-478 (Aharonian et al. 2006).



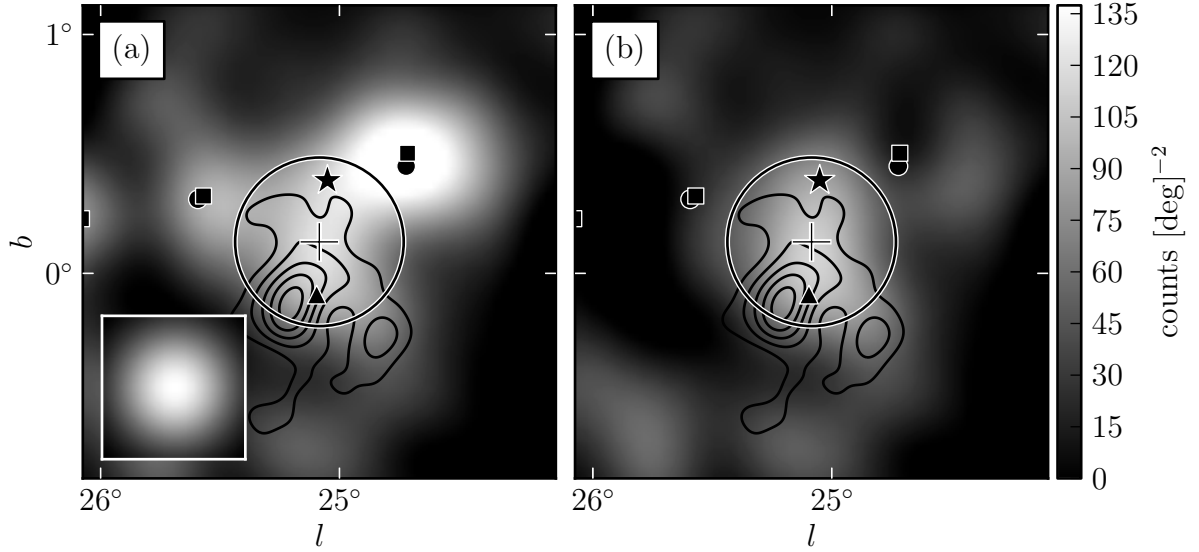


Fig. 20.— **A diffuse-emission-subtracted 10 GeV to 100 GeV counts map of the region around 2FGL J1837.3–0700c (a) smoothed by a  $0.15^\circ$  2D Gaussian kernel and (b) with the emission from the background sources subtracted.**

The triangular marker (colored red in the online version) represents the 2FGL position of this source. The plus-shaped marker and the circle (colored red) represent the best fit position and extension of 2FGL J1837.3–0700c assuming a radially-symmetric uniform surface brightness profile. The circular and square markers (colored blue) represent the 2FGL and the relocalized position of 2FGL J1839.3–0558c (left), 2FGL J1836.8–0623c (middle), and 2FGL J1834.7–0705c (right). The star-shaped marker (colored green) represent a 2FGL source that was removed from the background model. The contours (colored light blue) correspond to the TeV image of HESS J1837–069 (Aharonian et al. 2006).

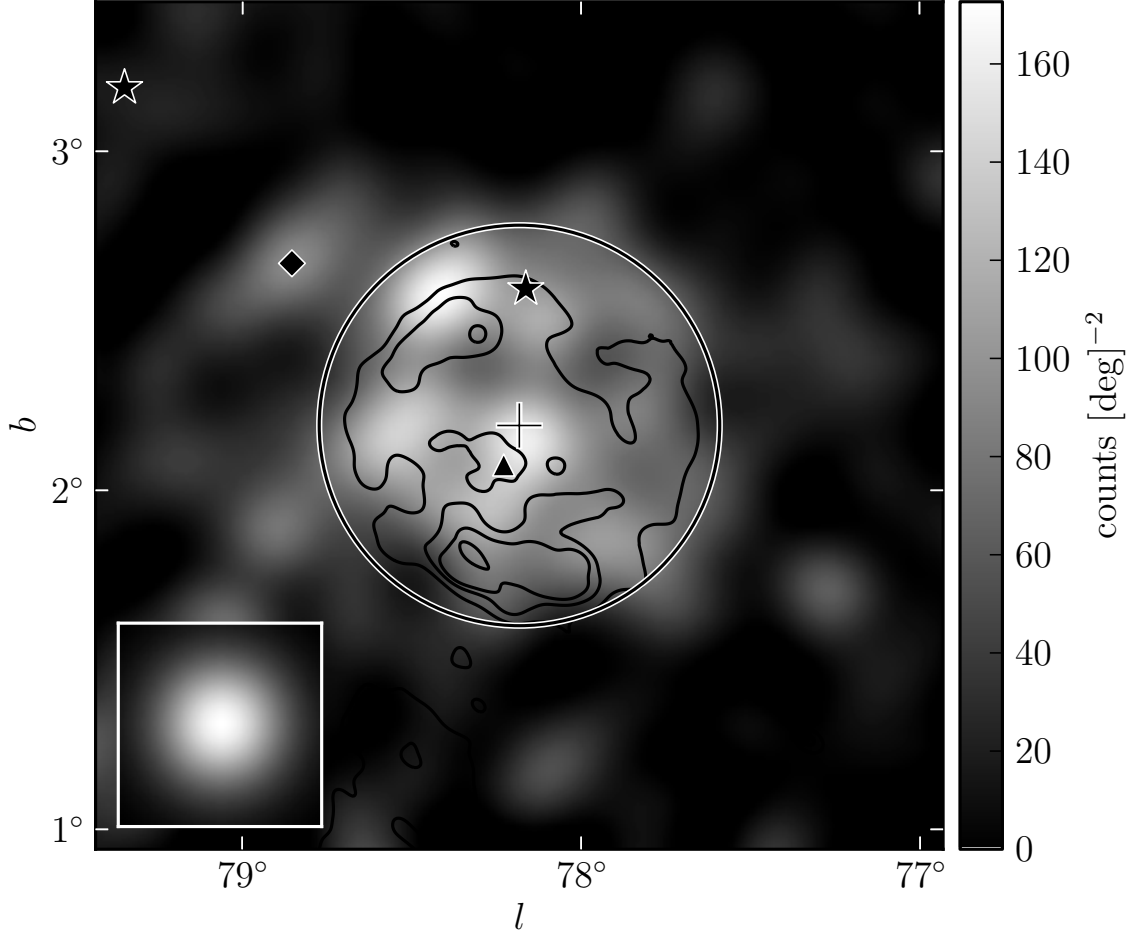


Fig. 21.— A Diffuse-emission-subtracted subtracted 10 GeV to 100 GeV counts map of the region around 2FGL J2021.5+4026 smoothed by a  $0.1^\circ$  2D Gaussian kernel. The triangular marker (colored red in the online version) represents the 2FGL position of this source. The plus-shaped marker and the circle (colored red) represent the best fit position and extension of 2FGL J2021.5+4026 assuming a radially-symmetric uniform surface brightness profile. The star-shaped markers (colored green) represent 2FGL sources that were removed from the background model. The diamond-shaped marker (colored purple) represents the position of a source not in 2FGL that was added to the region. 2FGL J2021.5+4026 is spatially coincident with the  $\gamma$ -Cygni SNR. The contours (colored light blue) correspond to the 408MHz image of  $\gamma$ -Cygni observed by the Canadian Galactic Plane Survey.

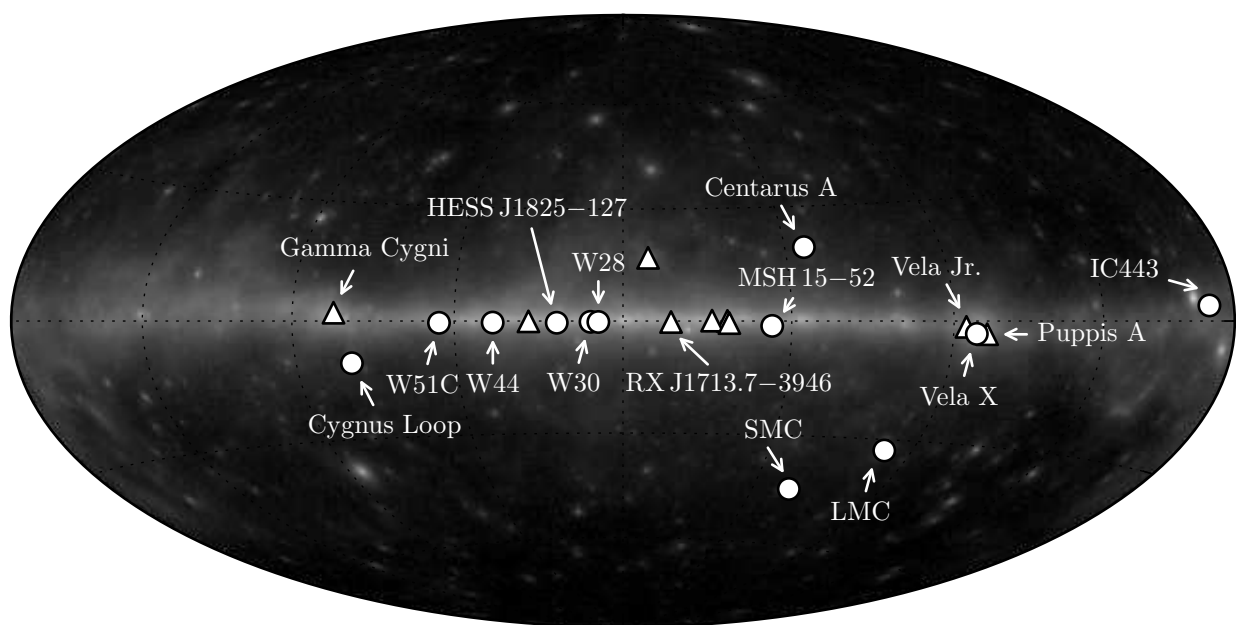


Fig. 22.— The 21 spatially extended sources detected by the LAT at GeV energies with two years of data. The twelve extended sources included in 2FGL are represented by the circular markers (colored red in the online version). The nine new extended sources are represented by the triangular markers (colored orange).

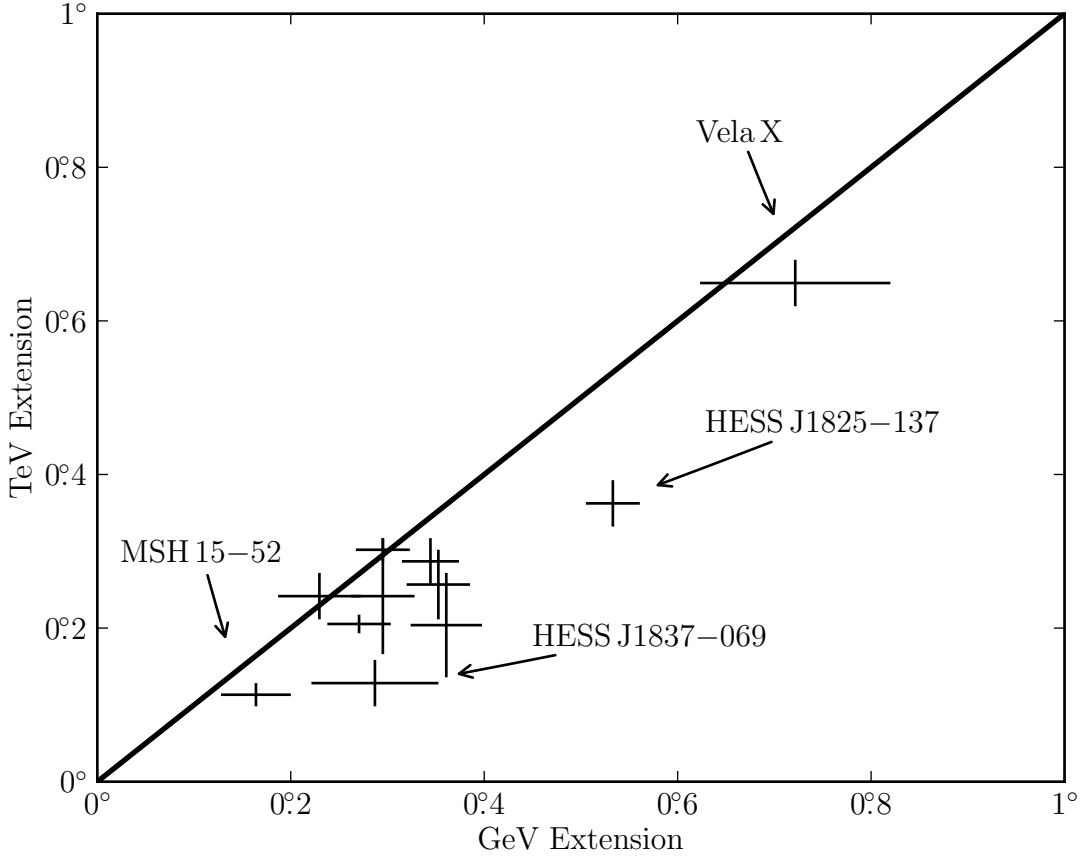


Fig. 23.— A comparison of the size of extended sources detected at both GeV and TeV energies. The TeV size of W30, 2FGL J1837.3–0700c, 2FGL J1632.4–4753c, 2FGL J1615.0–5051, and 2FGL J1615.2–5138 are from Aharonian et al. (2006). The TeV size of MSH 15–52, HESS J1825–137, Vela X, Vela Jr., RX J1713.7–3946 and W28 are from Aharonian et al. (2005, 2006b,c, 2007a,b, 2008). The TeV size of IC443 is from Acciari et al. (2009) and W51c is from Krause et al. (2011). The TeV size of MSH 15–52, HESS J1614–518, HESS J1632–478, and HESS J1837–069 have only been reported with an elliptical 2D Gaussian fit and so the assumed size is the average of the semi-major and semi-minor axis. The LAT extension of Vela X is from Abdo et al. (2010f). The TeV sources were fit assuming a 2D Gaussian surface brightness profile so the plotted GeV and TeV extensions were first converted to  $r_{68}$  (see Section 2.4). **Because of their large size, the shape of RX J1713.7–3946 and Vela Jr. were not directly fit at TeV energies and so are not included in this comparison. On the other hand, dedicated LAT publications on these sources showed that their morphologies are consistent (Abdo et al. 2011e,b).** The LAT extension errors are the statistical and systematic errors added in quadrature.

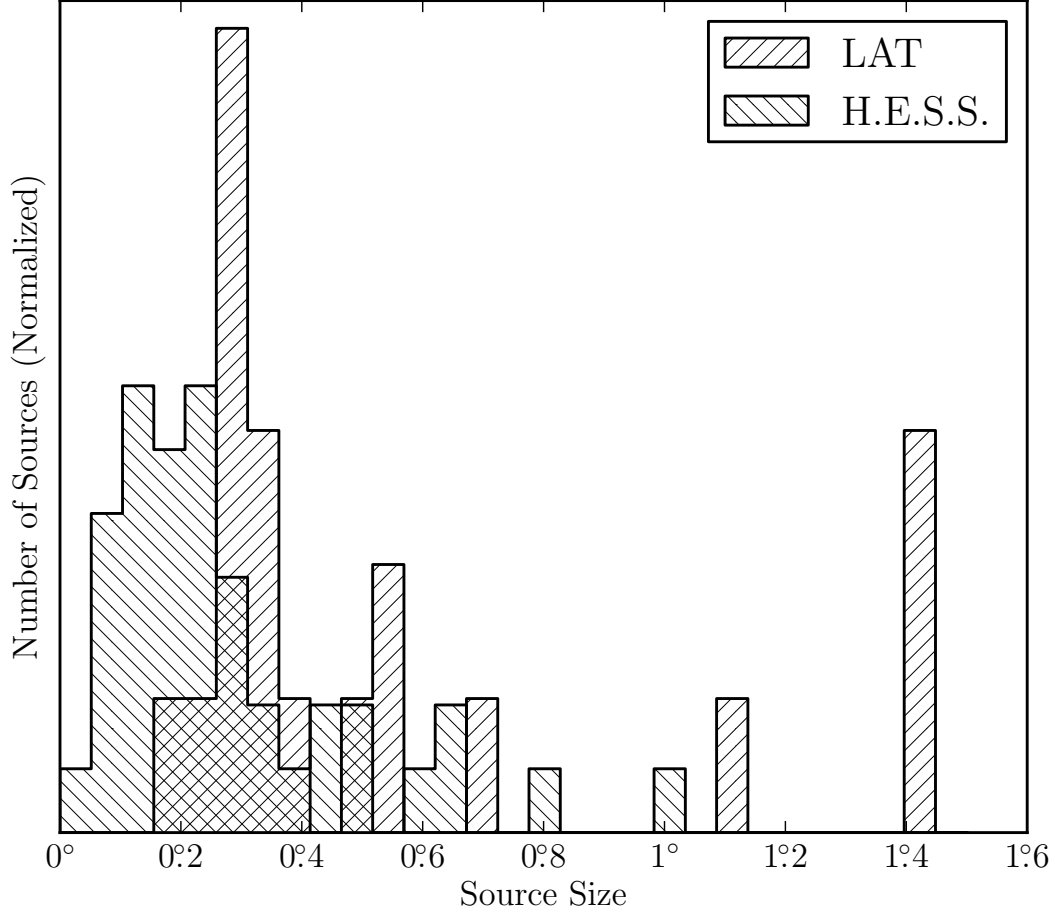


Fig. 24.— The distribution of the size of the 22 extended LAT sources at GeV energies (colored blue in the electronic version) and the size of the 42 extended H.E.S.S. sources at TeV energies (colored red). The size of Vela X is taken from Abdo et al. (2010f). Except for RX J1713.7–3946 and Vela Jr., the H.E.S.S. sources were fit with a 2D Gaussian surface brightness profile so the LAT and H.E.S.S. sizes are first converted to  $r_{68}$ . **Because of their large size, the shape of RX J1713.7–3946 and Vela Jr. were not directly fit at TeV energies. Their size at TeV energies is taken from the HESS source catalog to be  $0.5^\circ$  and  $1^\circ$  respectively. Because the spatial morphology of RX J1713.7–3946 and Vela Jr. is poorly described by a 2D Gaussian, the GeV and TeV extensions of these sources was not converted to  $r_{68}$ .**

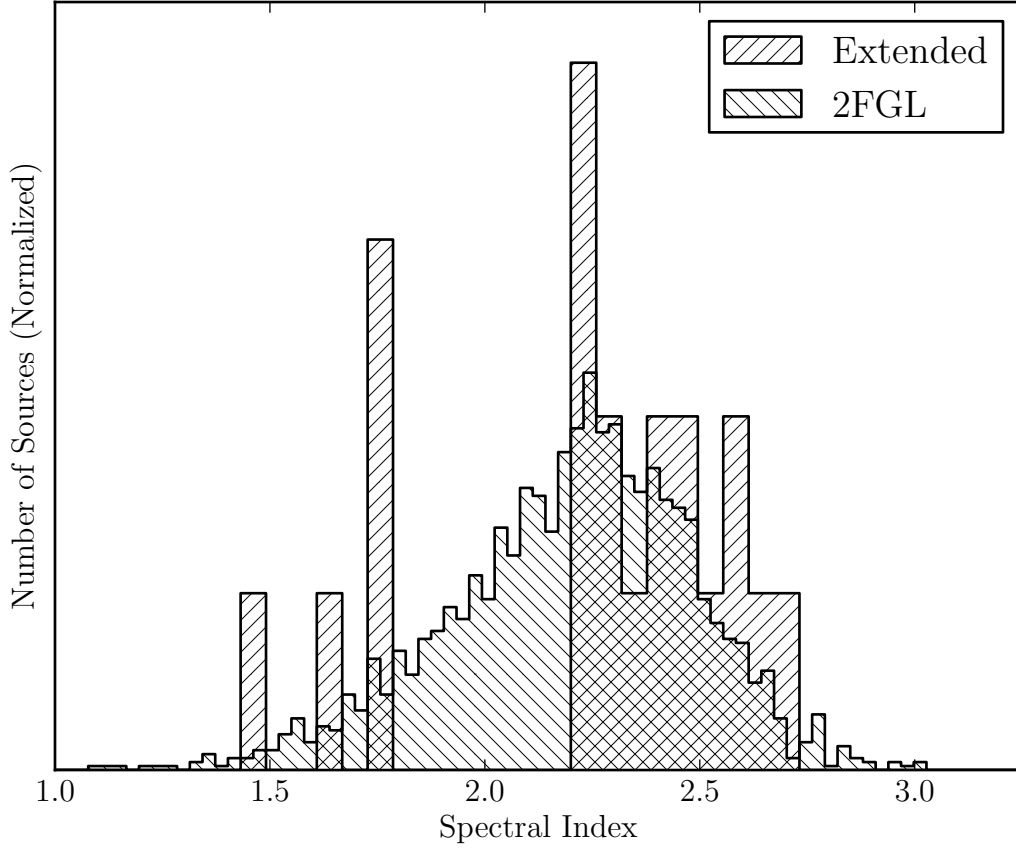


Fig. 25.— The distribution of spectral indices of the 1873 2FGL sources (colored red in the electronic version) and the 21 spatially extended sources (colored blue). The index of Centarus A is taken from Abdo et al. (2011d) and the index of Vela X is taken from Abdo et al. (2010f).